

REPORT DOCUMENTATION PAGE				Form Approved OMB No. 0704-0188	
<p>The public reporting burden for this collection of information is estimated to average 1 hour per response, including the time for reviewing instructions, searching existing data sources, gathering and maintaining the data needed, and completing and reviewing the collection of information. Send comments regarding this burden estimate or any other aspect of this collection of information, including suggestions for reducing the burden, to Department of Defense, Washington Headquarters Services, Directorate for Information Operations and Reports (0704-0188), 1215 Jefferson Davis Highway, Suite 1204, Arlington, VA 22202-4302. Respondents should be aware that notwithstanding any other provision of law, no person shall be subject to any penalty for failing to comply with a collection of information if it does not display a currently valid OMB control number.</p> <p>PLEASE DO NOT RETURN YOUR FORM TO THE ABOVE ADDRESS.</p>					
1. REPORT DATE (DD-MM-YYYY) 06/20/2007		2. REPORT TYPE FINAL		3. DATES COVERED (From - To) 02/15/2004-12/31/2006	
4. TITLE AND SUBTITLE Nan jets: Electrification, Energetics, Dynamics, Stability and Breakup				5a. CONTRACT NUMBER	
				5b. GRANT NUMBER FA9550-04-1-0093	
				5c. PROGRAM ELEMENT NUMBER 4106A46	
				5d. PROJECT NUMBER G-41-A46/R5233	
6. AUTHOR(S) Uzi Landman, Professor e-mail: uzi.landman@physics.gatech.edu				5e. TASK NUMBER	
				5f. WORK UNIT NUMBER	
7. PERFORMING ORGANIZATION NAME(S) AND ADDRESS(ES) Georgia Tech Research Corporation School of Physics, Georgia Institute of Technology, Atlanta, GA 30332-0430				8. PERFORMING ORGANIZATION REPORT NUMBER	
9. SPONSORING/MONITORING AGENCY NAME(S) AND ADDRESS(ES) Air Force Office of Scientific Research Scientific Contact: Dr. Michael R. Berman e-mail: michael.berman@afosr.af.mil AFOSR/NA, 875 N. Randolph St., Suite 325, Room 3112 Arlington, VA 22203 Phone: (703) 696-778				10. SPONSOR/MONITOR'S ACRONYM(S)	
				11. SPONSOR/MONITOR'S REPORT NUMBER(S)	
12. DISTRIBUTION/AVAILABILITY STATEMENT Approved for public release; distribution is unlimited					
13. SUPPLEMENTARY NOTES					
14. ABSTRACT Simulation methodologies, algorithms, and computer codes allowing molecular dynamics simulations of formation, propagation, and breakup processes of nan jets, generated either through the application of pressure or through the action of an electric field to liquids containing solvated charges, were developed. Particular emphasize was placed on simulations of electrically driven nan jets of liquid formamide solutions with dissolved NaI, and on investigations of the behavior and response of nanoscale drops of such solutions as well as of pure formamide, when placed in strong electric fields. The simulations, and coordinated electrospray experiments at the the AFRL, Hanscom AFB, demonstrated a mixed charge emission regime exhibiting field-induced cluster ion evaporation and ejection of charged droplets. The simulation average mass-to-charge ratios and maximal surface fields of about 1 V/nm agree with the experimental results and with electrohydrodynamic theory of cone-jets. The measured solvated ion distributions are also correctly reproduced by the simulations. Emission of charged particles is found in the simulations to occur predominantly from the tip of the nan jet, rather than from the neck between the Taylor cone and the nan jet. The simulations					
15. SUBJECT TERMS					
16. SECURITY CLASSIFICATION OF:			17. LIMITATION OF ABSTRACT UU	18. NUMBER OF PAGES 64	19a. NAME OF RESPONSIBLE PERSON Dr Uzi Landman
a. REPORT U	b. ABSTRACT U	c. THIS PAGE U			19b. TELEPHONE NUMBER (include area code) 404.894.3368

AFRL-SR-AR-TR-07-0211

FINAL REPORT

Nanojets: Electrification, Energetics, Dynamics, Stability and Breakup

Contract/Grant #: FA9550-04-1-0093

Reporting Period: 2/15/04-12/31/06

Prepared by:

Uzi Landman

School of physics

Georgia Institute of Technology

Atlanta, GA 30332-0430

Uzi. Landman@physics.gatech.edu

I. Summary

Simulation methodologies, algorithms, and computer codes allowing molecular dynamics simulations of formation, propagation, and breakup processes of nanojets, generated either through the application of pressure or through the action of an electric field to liquids containing solvated charges, were developed. Particular emphasis was placed on simulations of electrically driven nanojets of liquid formamide solutions with dissolved NaI, and on investigations of the behavior and response of nanoscale drops of such solutions as well as of pure formamide, when placed in strong electric fields. The simulations, and coordinated electrospray experiments at the AFRL, Hanscom AFB, demonstrated a mixed charge emission regime exhibiting field-induced cluster ion evaporation and ejection of charged droplets. The simulation average mass-to-charge ratios and maximal surface fields of about 1 V/nm agree with the experimental results and with electrohydrodynamic theory of cone-jets. The measured solvated ion distributions are also correctly reproduced by the simulations. Emission of charged particles is found in the simulations to occur predominantly from the tip of the nanojet, rather than from the neck between the Taylor cone and the nanojet. The MD simulations revealed novel field-induced structural ordering processes and electro-crystallization of pure formamide drops. The microscopic results obtained through the atomic-scale simulations were analyzed and compared to the predictions of a continuum formulation.

A detailed description of the molecular dynamics simulations of nanojet formation, field – induced cluster ion evaporation and charged droplet ejection is given in section IV, titled:

NANOJETS, ELECTROSPRAY, AND FIELD-ION EVAPORATION: MOLECULAR DYNAMICS SIMULATIONS AND LABORATORY EXPERIMENTS.

This section gives a summary of some of the main results obtained through the molecular dynamics simulations performed in the Center for Computational Materials Science at Georgia Tech, together with a description of coordinated laboratory experiments performed at the AFRL, Hanscom AFB, under the direction of Dr. R. A. Dressler.

II. Archival Publications

1. “Generation and Properties of Narrow Electron Beams in Mesoscopic Structures”, R.N. Gurzhi, A.N. Kalinenko, A.I. Kopeliovich, A.V. Yanovsky, E.N. Bogachek, Uzi Landman, Phys. Rev. B 72, 115332, (2005).
2. “Universality Crossover of the Pinch-off Shape Profiles of Collapsing Liquid Nanobridges in Vacuum and Gaseous Environments”, W. Kang and U. Landman, Phys. Rev. Lett. 98, 064504 (2007).
3. “Structured and Viscous Water in Subnanometer Gaps”, T.-D. Li, J. Gao, R. Szoszkiewicz, U. Landman, E. Riedo, Phys. Rev. B. Phys. Rev. B 75, 115415 (2007).
4. “Shape Transformation and Electrocrystallization of Polar Liquid Drops”, W.D. Luedtke, J. Gao and U. Landman, Phys. Rev. Lett. (2007).

5. “Nanojets, Electrospray, and Field-Ion Evaporation: Molecular Dynamics Simulations and Laboratory Experiments”, W. D. Luedtke, Y.-H. Chiu, D. J. Levandier, R. A. Dressler, S. Sok, M. S. Gordon, and U. Landman, J Phys. Chem. B, Feature Article (2007).

III. Researchers Supported by the Grant

1. Dr. Uzi Landman, Professor and Principal Investigator.
2. Dr. David Luedtke, Senior Research Scientist.
3. Dr. Jianping Gao, Senior Research Scientist
4. Mr. Wei Kang, Graduate Student

VI. Nanojets, Electrospray, and Field-Ion Evaporation: Molecular Dynamics Simulations and Laboratory Experiments

This section contains along with the results of the molecular dynamics simulations performed by W.D. Luedtke and U. Landman at the Center for Computational Materials Science at Georgia Tech, experimental results obtained by Y.-H. Chiu, D. J. Levandier, and R. A. Dressler, (Air Force Research Laboratory, Space Vehicles Directorate, Hanscom AFB, MA 01731-3010), and electronic structure calculations performed by S. Sok and M. S. Gordon (*Department of Chemistry, 1605 Gilman Hall, Iowa State University, Ames, IA 50011-3111*).

1. Introduction

Understanding the fundamental properties of conducting liquids under the influence of applied strong electric fields is a topic of continuing and growing interest. The associated phenomenology governs a number of venerable technological areas, most notably electrospray ionization,¹ electrospray propulsion,² electrospray painting, and electrospinning³ of materials. In all of these applications, the electric field causes deformation and charging of the liquid surface, with consequent phenomena including generation of jets, charged-droplet formation, Coulomb fission, and ion- field evaporation or desorption.

Coulomb fission of a drops occurs when the forces associated with Coulombic repulsion of surface charges exceed the forces associated with the liquid surface tension. The condition where the two forces are equal is referred to as the Rayleigh instability limit.⁴ Lord Rayleigh showed that the charge of a droplet at this limit is given by

$$q_R = (8\pi^2 \epsilon_0 \gamma d^3)^{\frac{1}{2}}, \quad (1)$$

where ϵ_0 is the permittivity of vacuum, γ is the surface tension of the liquid, and d is the droplet diameter. The electric field strength at the droplet surface in the absence of an external field is given by

$$E = \frac{q}{\pi \epsilon_0 d^2}, \quad (2)$$

and the critical field, E_R , is obtained from

$$E_R = \frac{q_R}{\pi \epsilon_0 d^2} = \sqrt{\frac{8\gamma}{\epsilon_0 d}}, \quad (3)$$

As discussed by Dole et al.,⁵ and subsequently by Iribarne and Thomson,⁶ large charged droplets of volatile liquids will evaporatively diminish in size (that is, reduce their diameter) while maintaining the charge, ultimately reaching the Rayleigh limit and undergoing Coulomb fission. In the model of Dole et al.,⁵ this process repeats itself until a charged solute residue is formed. Iribarne and Thomson explored the conditions at which the electric field strength at the surface of the droplet exceeds a threshold value, E_I , at which ion field evaporation occurs. This condition can be met provided $E_I < E_R(d)$

(otherwise Coulomb fission occurs), and the solid residue diameter is less than the critical diameter at which $E_I = E_R(d)$, i.e., in the case of salt solutions the concentration is low. E_I derives from the energy to overcome a barrier associated with the combination of the solvation energy of the evaporated ion, and the electrostatic interaction between the ion and the droplet. The estimates of Iribarne and Thomson⁶ put this barrier at about 4 Å from the surface.

Based on a kinetic model and charge mobility experiments, Thomson and Iribarne⁷ concluded that the critical field, E_I , was approximately 1 V/nm, and that field evaporation would be expected for droplets with diameters <10 nm. Loscertales and Fernández de la Mora⁸ and Katta and coworkers⁹ used charge mobility experiments and refined models to determine electric fields between 0.7 and 1.9 V/nm for the evaporation of different singly-charged ions. Fenn et al.¹⁰ also proposed similar fields by applying a simple electrostatic model to the interpretation of dilute polyethylene glycol solutions assuming that the charges of small droplets are equally spread on the droplet surface, and that the charge distances on the droplet cannot be less than that found on the multiply charged large field-evaporated ion. They determined fields ranging from 1.46 to 2.66 V/nm with increasing field strength required for smaller, less charged oligomer ions.

Since E_I does not directly depend on d , ion field evaporation should, therefore, also be a phenomenon observed from electrified jets. The detection and analysis of nascent ion currents from jets requires that the spray is in a vacuum, and consequently, such work is limited to liquids with low vapor pressures. Liquid metals, having very high surface tensions and, therefore high resistance to Coulomb fission, are known to produce intense metal ion beams in an electrospray configuration.¹¹ Jet formation does not occur under typical liquid metal electrospray conditions.

Organic solutions, the subject of this work, have significantly more flexible electrospray properties. For example, with such liquids one may observe a distribution of emitted ions, even under conditions where jet and charged droplet formation are favourable. Most of the early work on electrospraying organic solutions in a vacuum was conducted with glycerol. Huberman¹² conducted an energy analysis of positive ions sprayed from a NaI-glycerol solution, and detected a feature that was attributed to metastable solvated ions losing a solvent molecule. Stimpson et al.¹³ saw similar

behavior involving metastables in a mass spectrometric analysis of both positive and negative ions emitted from glycerol solutions of a number of salts. A large number of solvated ions as well as protonated glycerol ions were detected.

In the experiments by Huberman and Stimpson et al., the applied electrospray extraction voltage was very high, exceeding 8 kV. The high resulting fields are known to generate a stressed jet regime leading to multiple jets on the rim of the capillary orifice.¹⁴ In recent years, significant advances have been made in understanding electrosprays operating in a substantially more characterized single cone-jet mode, schematically depicted in Fig. 1.¹⁵⁻²⁴ Taylor²⁵ showed that the surface tension and electrostatic forces for a non-conducting liquid can balance in a way that leads to formation of a liquid cone with a well-defined half-angle of 49.3° at the cone apex. Such single cone configurations are now referred to as Taylor cones. Above a critical field, the cone becomes unstable and a jet is formed. Fernández de la Mora has derived a more general theory for single cone-jet sprays of conducting liquids predicting a broader range of cone apex angles which was also confirmed experimentally.¹⁵ The extraction voltages to operate in such a Taylor cone-jet mode are much lower, on the order of 1 to 2 kV, leading to a significantly gentler break-up of the jet. In ground-breaking work, Fernández de la Mora and Loscertales¹⁶ derived both theoretically and experimentally the proportionality between the parameters of a conducting liquid and the current emitted by the Taylor cone

$$I \sim (\gamma K Q / \varepsilon)^{\frac{1}{2}}, \quad (4)$$

where K and ε are the liquid conductivity and dielectric constant, respectively, and Q is the volume flow rate. It is noteworthy that no electrostatic parameters appear in the expression. The role of the external field is the generation of the Taylor cone and the associated surface-charge buildup. Eq. (4) can be rearranged in terms of specific charge of the emitted droplets, q/m ,

$$\frac{q}{m} \sim \frac{1}{\rho} \sqrt{\frac{\gamma K}{\varepsilon Q}}, \quad (5)$$

where ρ is the liquid density. Since droplets formed in jet fission are expected to be charged near the Rayleigh limit, the specific charge is also a measure of the diameter.

Thus, Eq. (5) states that the droplet size emitted by a Taylor cone can be controlled by parameters such as the liquid conductivity and the volume flow rate.

Inspection of the cone-jet structure in Fig. 1 allows the identification of 3 regions, the cone, the jet and the intermediate neck region. The latter represents the transition from a flow region in the Taylor cone, in which the electrostatic nonequilibrium associated with the narrowing cone diameter and increasing flow speed leads to ohmic currents within the liquid, to a convective flow region in the jet that is in electrostatic equilibrium, and where the charge density is lowered as the jet speed increases. Thus, the region of highest surface charge and normal electric field is in the intermediate neck region. Gamero-Castaño and Fernández de la Mora²² derived expressions for the maximum normal electric field and radius of curvature or jet radius in this region:

$$E_{\max} = \frac{\gamma^{\frac{1}{2}}}{\epsilon_0^{\frac{2}{3}}} \left(\frac{K}{Q} \right)^{\frac{1}{6}}, \quad (6)$$

$$R_{\max} = [\epsilon_0 Q / K]^{\frac{1}{3}}. \quad (7)$$

The above authors were also the first to observe field evaporation from a jet using NaI formamide solutions.²² Volume flow rates of less than 100 pl/s and conductivities exceeding 1 S/m were required, which lead to electric fields near 1 V/nm, fully consistent with earlier predictions of field evaporation onsets. Conditions were achieved at which the ion current exceeded the charged droplet current. At these conditions, the curvature of the transition region and the diameter of the jet are predicted to be in the vicinity of 10 nm. A cone-jet operated at these conditions can thus be classified as a nanojet.

Subsequently, ion field evaporation has been commonly observed with a third class of low-vapor pressure liquids, namely, ionic liquids.²⁶⁻²⁸ Particularly low flow rates can be obtained by replacing the capillary with a needle etched to optimize wetting properties.²⁹ Pure ion emission, signifying a vanishing jet, has now been observed for the ionic liquids [Emim][BF₄]²⁸ and [Emim][Im] (Emim: 1-3-ethyl-methyl-imidazolium; Im: 1-ethyl-3-methylimidazolium bis{trifluoromethylsulfonyl}imide),³⁰ whereby the former has been successfully sprayed using a micro-fabricated needle array.³¹ The

present paper, with a particular objective to learn about the liquid interface subjected to high electric fields, however, will focus on formamide salt solutions because of their more interesting variety of field evaporated ions, and because they are more tractable computationally. As demonstrated by the electrospray ionization community, the methodology is considered a soft-ionization approach. Thus, ion field evaporation at fields near the onset should be a gentle process producing ions that could reflect the microproperties of the solution at the interface, as was assumed by Fenn and coworkers in their analysis.¹⁰

Recently, Chiu et al.²⁸ conducted mass spectrometric analysis of positive ions emitted from a concentrated (28.4% weight) NaI-formamide solution operated in a Taylor cone-jet, field-ion evaporation mode. The measurements identified primarily solvated ions, $\text{Na}^+(\text{HCONH}_2)_n$, with a preferred solvation number of $n = 4$ which is the largest solvated ion predicted to be thermally stable at the room temperature. Thus the measurements appear to confirm the notion of a thermal evaporation process. Interestingly, however, the solvated ion energy distributions were found to be near or below the energies of the charged droplets, contrasting the electrohydrodynamic prediction that field ion evaporation would occur from the neck region of the jet which is expected to have a higher potential than the tip of the jet because of ohmic losses in the cone-jet transition region. Similar observations were made by Gamero-Castaño,²⁴ for the same solution. However, with measurements on the ionic liquid [Emim][Im] in a mixed ion/droplet regime, Chiu et al.^{32, 33} could demonstrate that field-evaporated ions clearly are emitted at the cone-jet neck, as evidenced by their energy and angular distribution, consistent with the theory advanced by Gamero-Castaño and Fernandez de la Mora.²²

Recent experimental and theoretical advances³⁴⁻³⁶ have shed new light on the interfacial properties of aqueous salt solutions (under conditions free of external electric fields). Counter to the long-held view that atomic ions are repelled by the air/water interface into the bulk, MD simulations of alkali-halide solutions have demonstrated that more polarizable anions reside preferentially at the liquid-to vacuum interface.^{34, 37-42} These results have been confirmed by X-ray photoelectron spectroscopy experiments,⁴³ as well as sum-frequency^{39, 40, 44, 45} and second-harmonic generation experiments^{36, 46-49} of aqueous halide solutions at ambient pressure. While these studies examine the

microscopic behavior of static solution interfaces, Vertes and coworkers⁵⁰ have conducted MD simulations of an acidic positive charged water nanodroplet, with the amount of excess charge taken near the Rayleigh limit. In these simulations field-ion evaporation of hydronium ions was observed; we note here that in these simulations negative ions were not included, and this may influence the properties of the simulated system, particularly at reduced dimensions.

We conclude our brief review of recent work with the MD simulations, performed by Moseler and Landman⁵¹, of liquid flows at nanoscale dimensions, and the formulation of a stochastic hydrodynamic treatment. In these studies simulations were performed of liquid propane flowing under applied back-pressure through a cylindrical tube, and emanating through a nanoscale nozzle into a vacuum; recently Kang and Landman have extended these simulations to injection of liquid jets into a surrounding fluid (W. Kang and U. Landman, Phys. Rev. Lett. 98, 064504-1 – 64504-4 (2007)). The properties of the resulting jets – in particular the characteristics of the breakup of the liquid jet into droplets - were found to differ from continuum hydrodynamics predictions. It was discovered that a newly derived hydrodynamic formulation that includes intrinsic size-dependent fluctuations, provides a faithfully accurate description, in agreement with the atomistic simulations. This work lays the groundwork for an investigation of electrospray jets, where the cone-jet transition region can be regarded as a virtual, nanoscale nozzle.

In this paper we present a systematic study of field ion evaporation from salt solutions using a combination of mass spectrometry and MD simulations. To gain insights into the microscopic processes of nanojet formation and charge emission from dielectric liquids under the influence of strong electric fields we chose to investigate theoretically the behavior and response of liquid drops (made of pure formamide or NaI s formamide solutions), since studies on such system frees us from complicating factors, including considerations of effects due to flow rates, contact angles, and the geometry of the capillary tube ,or needle, used to generate the slender liquid flowing system. The MD simulations were conducted on a 10 nm diameter, uncharged (equal amount of positive and negative charges) NaI-formamide droplets subjected to external electric fields with strengths on the order of 1 V/nm. The size of the drop was selected such that the corresponding curvature of the droplet ($1/R$) would be comparable to the estimated

minimum curvature expected to be encountered on a liquid jet (see Eq. (7)), and thus the physics of jet formation, ion field evaporation, and charge emission from such drops can be taken as representative of the processes occurring in electric field-driven cone-jet flow systems. Indeed, experimental results of field-induced dual-jet formation on droplets, either flowing through a region of high electric field or levitated, have been reported⁵²⁻⁵⁵; these studies relied on visual/optical examination and were conducted on droplets with diameters exceeding 50 μm exhibiting formation of jets. Under these conditions field-ion evaporation from the main drop is not expected to occur. We remark here that Grimm and Beauchamp conducted mass spectrometric measurements of field evaporated ions from droplets of methanol solution that are ejected from larger (170 μm diameter) drops.⁵⁵ However, the high external fields that would be required to induce direct field evaporation from 10 nm diameter droplets (which, as noted above, is the size range of interest to us here) were outside the range of these earlier experiments.

The mass spectrometric measurements presented in this paper were conducted on ions that are field evaporated from a cone-jet of solutions (NaI dissolved in formamide) with similar concentrations to those examined in the simulations. Quantum chemical calculations were carried out to determine the energy-optimal structures and thermochemistry of solvated ion clusters with sizes equals to those observed experimentally. The thermochemistry and associated normal mode frequencies are used to assess the thermal stabilities and lifetimes of the ions. The solvated ion cluster lifetimes are of particular importance for our analysis because they are used in extrapolating and comparing the simulated results concerning mass distributions of emitted solvated ions (that are simulated for relatively short flight times) to the experimental, mass spectrometric data, obtained for much longer flight times. Both positive and negative solvated ion distributions, obtained experimentally from respective positive and negative extraction fields, and from calculated evaporation statistics at opposite ends of the simulated droplet, are presented and analyzed.

2. Experimental

The mass spectrometric experiment has been described in detail previously,²⁸ and only the features relevant for this article will be discussed. A schematic of the apparatus is

shown in Fig. 2. The electrospray source consists of a tapered 5 μm inner diameter fused silica capillary tip (New Objective, Inc.) that is fed by a 50 μm inner diameter transport capillary via a capillary union (Upchurch Scientific). The solution flow rate is controlled by pressurizing the liquid reservoir supplying the transport capillary with dry nitrogen. The flow rate is determined from the velocity of bubbles introduced into the liquid near the transport capillary entrance. The capillary tip is positioned within 1 mm of an extractor electrode with an orifice of 6 mm diameter. The tip and extraction optics are all in a vacuum ($<10^{-6}$ Torr). Typical extractor voltages used for the 28.4 wt% NaI-formamide solution were 2 kV. The capillary bias voltage was applied to the capillary through a metal layer that coated both the inner and outer surface of the capillary at the entrance end. Typical bias potentials were 450 V, while the extractor was biased at -1,550 V for positive polarity, and the reverse for negative polarity. These voltages were chosen to minimize the ion energy in the mass filter, while maintaining reasonable ion transmission through the apparatus.

The charged particle beam extracted from the capillary tip can either be focused on a near-field target consisting of an interchangeable Faraday cup, or a quartz crystal microbalance (QCM; XTM/2, Inficon), or towards the entrance of a quadrupole mass filter. The near-field target is used for general characterization of the charged-particle beam through total current and mass flow measurements. The ratio between mass flow and current provides the average m/q value, which, in conjunction with ion mass distribution measurements, provides a measure of the fraction of charged droplets in the beam. The near-field target is translated away from the beam axis for mass spectral measurements. Given the possibility of broad ion energy distributions, the quadrupole filter is the mass spectrometer of choice since the quadrupole mass setting is independent of energy. However, the mass resolution declines with ion energy. Following transmission through the quadrupole, the ions pass through a retarding potential analyzer prior to being detected using a channel electron multiplier. The retarding potential analyzer is used to measure the energy distribution of mass selected ions.

Mass calibration, the mass transmission function and detector response are obtained from mass spectra of a standard calibrant compound, FC-43, with a known fragmentation pattern at an electron energy of 70 eV. The spectra were obtained after

replacing the electrospray source with an electron-impact ionization source. The intensities of fragmented ions of FC-43 were measured for all investigated quadrupole transmission energies, from which the mass-dependent discrimination correction factors were determined.

The concentrated 28.4 wt% and 1/4 volumetrically diluted NaI-formamide solutions used in this study have salt to formamide mole ratios of 1:8.4, and 1:36.9, respectively. Similarly, the salt/formamide mole ratios determined for KI/Formamide solutions in this study are 1:40.9 and 1:83.0, respectively. The measured conductivities for the concentrated and dilute NaI-formamide solutions are 1.64 S/m and 1.26 S/m, respectively; conductivities of 1.32 S/m and 0.77 S/m are found for the concentrated and dilute KI/Formamide solution.

3. Computational methods

3.1 Molecular dynamics simulations

To enable large-scale atomistic simulations of the thermodynamic and electrohydrodynamic properties of complex fluids (with large partial and ionic charges) under the influence of strong electric fields a computer code with parallel architecture was developed. To model these systems faithfully, it is important to treat the long-range coulombic interactions accurately and efficiently. In our initial studies of pure formamide droplets, long-range Coulombic interatomic potentials were treated with finite interaction cut-offs ranging from 1 to 4 nm. The use of finite range cutoffs inhibited the expected droplet elongation as predicted by continuum theory⁵⁶ of dielectric drops. Coulombic interactions had to be treated much more accurately (namely no cutoff) to bring the simulation results into qualitative agreement with existing continuum theory. Obviously, the addition of ionic species further increases the necessity of proper implementation of long-range Coulomb interactions. Indeed, the more accurate treatment of dipole-dipole and dipole-field cooperative interactions then allowed droplets to respond correctly to external fields including field-induced polarization, elongation, and instabilities resulting in emission of charged cluster ions and electrified jets.

The long-range forces were modeled in these simulations through the use of the fast multipole method (FMM)⁵⁷ specifically formulated and programmed for a parallel architecture and adapted to the present problem. The FMM method enables the modeling of large systems with long-range interactions by using a “tree-structure” subdivision of cells that allows a charge to interact with a small set of multipoles representing entire, increasingly larger, volumes of remote space, rather than with all of the individual charges contained within the cells. Important features of the program developed for this study are:

1) The ability to replicate basic root-cells and “stack” them along a particular axis to create a long narrow tree-structure. This is particularly useful for efficient simulations of systems such as highly elongated droplets and long liquid jets.

2) A large degree of flexibility in the choice of boundary conditions (bc’s). The computer program allows the implementation of periodic boundary conditions (pbc’s) in one, two or three spatial directions, or the execution of “cluster simulations” where pbc’s are not imposed altogether. In simulations using pbc’s in less than 3 directions, the non-periodic directions can be reflecting (closed systems) or absorbing (open system). Absorbing bc’s (any atoms that cross the system boundary are removed from the simulation) are necessary in simulations of fragmenting droplets or liquid jets where there are large fluxes of atoms crossing the finite boundaries (keeping these atoms in the root-cell would cause artificial effects).

3) A modified FMM algorithm so that, when using pbc’s, the tree-structure of the root-cell, along with all its computed multipoles, can be replicated a specified number of times as neighboring image cells. When this is done, atoms in the central computational cell see the correct multipole structure as they interact with neighboring periodic image cells out to any desired distance.

4) The ability to perform constant pressure simulations. The spatial dimensions of the root-cell can be allowed to vary, while using three-dimensional pbc’s and the FMM, according to a modified constant-pressure algorithm due to Berendsen.⁵⁸ Bulk samples of both crystals and dielectric fluids can, therefore, be prepared with solvated ionic salts at any pressure or temperature of interest.

In the droplet simulations of this work, the basic root-cell of the FMM code has 8 tree levels with the smallest leaf cell chosen to be 1.2 nm on each side. This gives a root-cell of $2^{(8-1)} * 1.2 \text{ nm} = 153.6 \text{ nm}$ dimensions on each side. For the studies of droplet response to a constant external electric field, this root-cell is replicated 3 times along the z-axis (the electric field direction) to give a total tree-structure of 153.6 nm x 153.6 nm x 460.8 nm in the center of which we place the 10 nm diameter droplet. The very large system size allows enough room for the parent droplet to move and elongate freely with sufficient time for charged cluster emission. Once the simulation begins, no form of temperature control or control of the droplets center-of-mass motion is performed to minimize the risk of introducing artificial effects.

Given the size of the present droplets, it is important to utilize an efficient, simple representation of the inter-atomic forces. Formamide is treated as a solid body with quaternion dynamics,⁵⁸ implemented using a mid-step implicit leap-frog algorithm⁵⁹ that has been shown to be an extremely stable integration scheme with minimal energy drifts for long simulation periods. The geometry of the formamide molecule is taken from high-resolution X-ray studies of formamide crystals.⁶⁰ The AMBER force field parameters⁶¹ were used to describe the intermolecular van der Waals interactions between formamide molecules, the interactions between the formamide molecules and the atomic ions, as well as the ion-ion interactions. CHELP-BOW partial atomic charges⁶² were used for the overall description of the electrostatic potential of the formamide molecules. While long-range Coulombic interactions between formamide molecules were not truncated, the weak van der Waals interactions were truncated on a group (molecular) basis through the use of a smooth switching function described by Perera et al.⁶³

3.2. Quantum chemical methods

3.2.1 Solvated positive ions

We have conducted density functional theory (DFT) calculations of the observed positive solvated-ion structures to estimate their thermal stability and the dissociation energies associated with loss of 1 formamide solvent molecule. Calculations were performed at the B3LYP/6-31G(d) level using the Gaussian 98/Gaussian 03 quantum chemistry

package.⁶⁴ Geometries were optimized, and normal-mode frequencies for zero-point energy determinations were calculated for solvated ions of $[\text{Na}^+(\text{HCONH}_2)_n]$ and $[\text{K}^+(\text{HCONH}_2)_n]$, where $n=1-6$.

3.2.2 Solvated negative ions

Initial geometry optimizations of $[\Gamma(\text{NH}_2\text{CHO})_n]$, $n=1, 5$ were performed using an augmented correlation consistent double zeta basis set for second row atom,⁶⁵ 6-31G basis set for hydrogen,⁶⁶ Radom ECP basis set for iodine,⁶⁷ and the B3LYP⁶⁸⁻⁷⁰ functional. These geometries were then refined with Møller-Plesset second-order perturbation (MP2) theory⁷¹⁻⁷³ and the 6-311G+(d,p)⁷⁴ basis set using the Radom 6-311+G(df) basis set for iodine.⁷⁵ Gradient convergence tolerance for geometry optimizations was set to 10^{-6} Hartree/Bohr. Stationary points were characterized by a positive definite Hessian (matrix of energy second derivatives). Harmonic zero-point energy and temperature corrections (to 298.15K) were obtained using the MP2 Hessians. All calculations were performed using the June 27, 2005 (R3) version of GAMESS (General Atomic and Molecular Electronic Structure System).^{76, 77}

3.3 Unimolecular ion dissociation rate calculations

The distributions of the measured ion solvation numbers (that is, the distribution function the number of solvating foramide molecules in a solvated-ion clusters) deduced from the measurements, are compared with predictions based on the assumption that the ions are evaporated from a liquid at or near room temperature. As the solvation number increases the energy for loss of a single solvent molecule reduces, while the internal energy of the solvated ion increases. Above a certain solvation number, a fraction of the internal energy exceeds the dissociation energy of the solvated ion, making the respective ions thermally unstable. Using the normal mode frequencies from the ab-initio calculations, we determine the thermal internal energy distributions of the observed solvated ions from the relation

$$F(E_{\text{int}})dE_{\text{int}} = F_{\text{rot}}(E_{\text{rot}})F_{\text{vib}}(E_{\text{vib}})dE_{\text{rot}}dE_{\text{vib}}, \quad (8)$$

where $F_{rot}(E_{rot})$, and $F_{vib}(E_{vib})$ are the normalized rotational and vibrational Maxwell-Boltzmann energy distribution functions for a temperature, T , and

$$E_{int} = E_{rot} + E_{vib}. \quad (9)$$

For those ions with internal energies exceeding the binding energy, we determine the unimolecular dissociation rate using a RRKM approach, employing following the methodology developed by Hase and coworkers.⁷⁸ Due to the large dipole of formamide (3.7 D) and the resulting strong attractive interaction between the solvated ion and the solvating ligands, there is no centrifugal barrier to dissociation and a very loose transition state is assumed. We assume conditions near the phase space limit, and the transitional vibrational modes are treated as rotors, as prescribed by Rodgers et al.⁷⁹ All systems considered include a single solvation shell and, given the shallow global minima, and near symmetry of the normal mode frequencies, all ligands are treated equivalently. All rotors are treated as active in both the reactant and transition state, vibrational states are treated as harmonic oscillators, and the sum and density of states are determined using the Beyer-Swinehart direct count algorithm.⁸⁰ Adiabatic treatment of both reactant and transition state rotors does not markedly change the results.

The survival fraction, $P(n, T)$, of ions of a particular solvation number, n , at a temperature, T , is then determined from the expression

$$P(n, T) = P_s(n, T) + \int_{E_0}^{\infty} P_m(n, T, E_{int}) e^{-k(E)\tau} dE_{int}, \quad (10)$$

where $P_s(n, T)$ is the fraction of stable ions with internal energies below the dissociation limit, E_0 ; $P_m(n, T, E_{int})dE_{int}$ is the fraction of ions with energies in an interval $E_{int} + dE_{int}$; $k(E_{int})$ is the unimolecular dissociation rate constant, and τ is the average flight time of the respective ions in the mass spectrometric apparatus described in Section 2. The experimental flight times are on the order of 25×10^{-6} s.

4. Results

4.1 Mass spectrometric measurements

Single cone-jet sprays were generated for the concentrated and dilute NaI formamide solutions. The operational parameters of the experiments are summarized in Tab. 1. For the 28.4% wt. (1:8.4 mole ratio) concentrated solution, the extraction voltage was 2,000 V for both polarities, while a slightly higher voltage was necessary for stable operation of the dilute (1:36.9 mole ratio) solution. The measured charge emission currents correspond to $I(\text{total})$. The ratio between the Faraday Cup current, $I(\text{Faraday Cup})$, to the emission current provides a measure of the beam divergence. Mass flows registered by the QCM detector are also listed. The average charged particle mass-to-charge ratio, m/q , is then derived from the ratio of mass flow to Faraday Cup current.

Comparison between the total emission current and that recorded on the Faraday cup that collects a solid angle close to that of the QCM allows an assessment of the electrospray divergence. The measured divergence markedly higher measured divergence for the concentrated solution can be attributed to the lower acceleration voltage and the higher current density, as well as possible modification of the emission physics at the cone-jet. This will be further elaborated on in the discussion section.

The large m/q values suggest that for both solution concentrations the cone-jet emits in a mixed droplet/ion regime, where the main fraction of the mass flow is carried by the droplets, while a substantial fraction of the current comes from ions generated via the field ion evaporation mechanism. This is verified by a calculation of the maximum electric field and the corresponding characteristic radius of curvature according to Eq. (6) and (7). The flow rates, Q , were obtained from the mass flow assuming a density of 1.13 g cm^{-3} . The surface tension of pure formamide, 0.0575 N m^{-1} , was assumed for the calculation of E_{max} . Note that Eqs. (6) and (7) are based on the total flow rate so that the derived values based on the mass flow recorded by the QCM must be regarded as upper (E_{max}) and lower (R_{max}) limits. Depending on the charge emission dynamics, it is possible that the angular m/q distributions exhibit a certain degree of non-uniformity. The determined representative maximum electric field strength ranges from 1.42 and 1.7 V/nm, with higher fields corresponding to the concentrated solution, while the jet

dimensions are associated with radii in the range between 2.3 and 3.29 nm, with the larger radii determined for the dilute solution.

The negative total emission currents tend to be almost twice as high as those observed for positive charge emission. Two significant differences are observed for the dilute solution in comparison with the concentrated one: (i) for the former the total emission current is lower, while the fractional current registered on the Faraday Cup is higher, signifying a less divergent spray, and (ii) the negative ion average mass-to-charge ratio is higher for the more dilute solution, while the positive ion mass-to-charge ratio does not change significantly upon dilution.

Figure 3 shows positive and negative ion mass spectra recorded for the concentrated, 28.4% wt. NaI-formamide solution. The spectra have been corrected with respect to the mass spectral transmission function. The low mass resolution can be attributed to the high transmission energies of 550 eV. The most abundant positive ion mass can be primarily attributed to the solvated sodium ions, $\text{Na}^+(\text{HCONH}_2)_n$, whereby the $n = 4$ solvated ion is the most abundant positive ion species. Minor contributions to the mass spectrum, attributed to the formation of $\text{Na}^+(\text{NaI})(\text{HCONH}_2)_m$, are also observed. The individual abundances are determined by fitting to the observed peaks Gaussian mass distributions given by the experimental resolution at the expected peak positions. The derived normalized abundances are listed in Tab. 2. Also shown is the Na^+ solvated ion distribution determined for the 1/4 volumetrically diluted solution. The abundances are essentially identical to those of the concentrated solution except for higher abundances at the highest solvation numbers. Interestingly, at the lower concentration complex $\text{Na}^+(\text{NaI})(\text{HCONH}_2)_m$ ions could not be detected with sufficient accuracy to allow a definite identification.

When applying an extraction field with a negative polarity, the main observed ions are solvated iodine anions, $\text{I}^-(\text{HCONH}_2)_n$, with a distribution peaking at $n = 2$. Minor intensities of $\text{I}^-(\text{NaI})(\text{HCONH}_2)_m$ are also observed. The abundances are listed in Tab. 3. Contrary to the Na^+ positive ions, dilution has a marked effect on the observed solvated I^- mass spectrum, where broadening of the distribution is observed with a peak at $n = 5$. Similar to the positive ions, the more complex ions, $\text{I}^-(\text{NaI})(\text{HCONH}_2)_m$, are not detected upon dilution.

Mass-resolved retarding potential measurements are shown in Fig. 4 for $\text{Na}^+(\text{HCONH}_2)_4$ and high mass ($m/q > 400$ amu) emitted charged particles obtained by operating the quadrupole in an rf-only high-pass mode. The capillary potential was biased at 550 V while the retarding grid analyzer was at ground (see Fig.2 for a schematic of the experimental setup). From these measurements we conclude that charged droplets are formed at a potential ~ 200 V below the capillary potential, while the solvated ions are formed with a broader energy distribution centered slightly below the droplet appearance energy, with a minor contribution at higher energies. The distributions look very similar for ions with other solvation numbers. Meanwhile, the energy distributions do not change noticeably for negative ions and the dilute solution.

Although no simulations were carried out for KI solutions, we found it useful for comparative purposes to also investigate mass spectrometrically KI/formamide solutions. A solution at the same weight concentration as the concentrated NaI solution froze or crystallized at the capillary orifice and no measurements could be carried out. We succeeded in creating stable cone-jets with 1/4 volumetric diluted and 1/8 volumetric solutions at extraction voltages of 2100 V and 2300 V, respectively. The same corresponding solvated ions were observed, and the abundances are listed in Tables 4 and 5. As for the Na^+ ions, the simple solvated K^+ ions have distributions that are not greatly affected by dilution, with peak at $n = 5$, and significantly higher abundances at larger solvation numbers than observed for Na^+ . Complex ions, $\text{K}^+(\text{KI})(\text{HCONH}_2)_m$, are generally more abundant than in the NaI solutions, and are observed for both dilute solutions. The solvated anion distributions show the same trend of peaking at higher solvation numbers upon dilution as observed for the NaI solutions. Contrary to the dilute NaI solution, complex anions are also observed for the KI solutions.

4.2 Solvated ion thermochemistry and ion survival fractions

The binding energies of the calculated solvated ions, $\text{Na}^+(\text{NH}_2\text{CHO})_n$, $n = 3-6$, and $\text{I}^-(\text{NH}_2\text{CHO})_n$, $n = 2-5$, determined from the quantum chemical calculations, are shown in Table 6. Also listed are the zeropoint energies, E_{zpe} , and the internal energies, E_{int} , above the zeropoint energies at 298.15 K (difference between thermal energy and zeropoint energy). We find that the internal energy at 298.15 K exceeds the binding energy above

$n = 4$ for the cationic solvated ions, and $n = 3$ for the Γ^- solvated ions, respectively. Table 6 also lists the corresponding classical values determined for the clusters bound by the interatomic potentials used in the MD simulation. In the case of the Na^+ clusters, the MD binding energies are significantly lower than the quantum chemical values at low n with improved agreement as n increases. The agreement is generally good between the MD binding energies and the quantum chemical values for the Γ^- clusters. The MD internal energies correspond to the total cluster kinetic and potential energy minus the minimum potential energy, with the exclusion of the kinetic energy associated with the center-of-mass velocity. The energies are obtained from averages over random samples of clusters taken from separate MD simulations of such cluster ensembles thermalized initially at 310 K. As is evident that the onset of thermal instability is for clusters with the number of formamide ligands above $n = 5$ for Na^+ and $n = 4$ for Γ^- ions. The satisfactory agreement with the quantum chemical predictions supports the conclusions that we drew from comparison between the experimental and the MD results about the properties of the field-evaporated ions.

Table 7 lists the thermal ion survival fractions calculated for selected $\text{Na}^+(\text{NH}_2\text{CHO})_n$ ions evaporated with characteristic temperatures of 300, 350 and 400 K. The survival fractions are calculated for infinite observation times, mass spectrometer flight times, and the MD simulation flight time of ~ 15 ps, and are based on the RKKM-type unimolecular dissociation rate calculations described in Section 3.2. The corresponding survival fractions for selected $\Gamma^-(\text{NH}_2\text{CHO})_n$ ions are given in Table 8.

4.3 Molecular dynamics simulations

Dielectric and charged droplets in uniform electric fields are well-studied problems involving electrified fluids.^{4, 25, 52-55} The salient features of the physics associated with electrosprays operating in the cone-jet mode may be seen already in the simpler problem of a conducting liquid droplet elongated in a uniform external electric field, including the formation of electrified jets, as well as the emission and acceleration of charged species at the ends of the elongated parent drops. Indeed, Taylor²⁵ studied the instabilities and jet formation of fluids emerging from an electrospray device as a way to investigate in a

more controlled manner the physics related to the elongation and jet formation of droplets in a uniform electric field.

In light of the above, atomistic molecular dynamics (MD) studies were initiated of field-induced fluid instabilities relevant to the operation of electrospray devices by studying first the closely related phenomena present in the behavior of dielectric droplets, with and without dissolved salts. As discussed below, the results of the MD simulations complement and agree with the experimental electrospray results to a high degree. First, we present results from the study of pure formamide droplets, of the same size as the formamide/NaI solution droplets that are our primary focus.

4.3.1 Simulations of pure formamide

Since the potential parameters employed in our simulations were not specifically developed to reproduce certain physical properties of the simulated formamide (such as the melting point and dielectric constant) it was necessary to perform preparatory simulations to ascertain the physical behavior of the simulated liquid formamide. Constant pressure simulations and liquid-solid coexistence studies⁸¹ indicate that our description of formamide yields a liquid density that is to within a few percent of the experimental value, and a melting point that is approximately 10 K above the experimental value of 275 K. For an improved comparison with experiment, and to avoid freezing of the field-evaporating salt solution droplets, the simulations are, therefore, performed at 310 K (that is, 10 K above the experimental conditions).

The droplets used in our simulations were created by ‘carving out’ a spherical region from an equilibrated bulk liquid simulation that was performed at constant temperature and zero pressure, with a subsequent equilibration prior to the application of an external field. The diameter of the spherical droplet chosen for the MD simulations is 10 nm and it contains 7150 formamide molecules (each molecule comprised of six atomic partial charges). This droplet is large enough to allow meaningful comparison with continuum electrohydrodynamic theories, and in addition its curvature is similar to the estimated local curvature of the experimentally probed liquid jet at the place where the electric is maximal (see Eqs. 6 and 7). From a practical point of view, the chosen

droplet size is sufficiently small to allow a wide range of computer experiments to be performed in a reasonable amount of time.

The droplet was equilibrated in a range of increasing electric field strengths (from 0 to 3 V/nm). The effect of the externally imposed electric field can be seen in Fig. 5 where we display snapshots of the droplet for three values of the applied field, illustrating instability at a critical electric field strength. At field strengths below ~ 0.5 V/nm, the droplet undergoes mild elongation with increasing field strength. At a field strength of 0.625 V/nm the droplet becomes unstable and undergoes a pronounced elongation resulting in a change in aspect ratio ($\eta = c/a$, where c and a are the major and minor axis of the ellipsoid) from $\eta \sim 1$ to $\eta \sim 13$. The elongation is also reflected in changes in the average molecular dipole moment projected onto the z axis. There have been a number of studies addressing the critical external field at which a dielectric droplet displays this instability. In early work, Taylor²⁵ theoretically predicted that a droplet of initial radius R (in zero external field) becomes unstable at an external field strength, $E_{critical}$, satisfying (MKS units):

$$E_{critical} = 1.625(\gamma / 2\pi\epsilon_0 d)^{1/2}, \quad (11)$$

Applying $\gamma = 0.046$ N/m for the surface tension of the present droplet (computed in separate simulations)⁸¹ and $d = 9.68$ nm for the computed equimolar diameter, results in a predicted critical applied electric field of $E = 0.48$ V/nm which is only slightly lower than the interval of 0.5-0.625 V/nm in which the instability is observed to occur in the MD simulation. We note that if the experimental surface tension⁸² $\gamma = 0.0575$ N/m is used, the predicted critical field strength is 0.53 V/nm. We conclude that a continuum formalism provides an adequate description of our results obtained for nanometer scale droplets. Additionally, it was discovered⁸¹ that the external electric field can induce crystallization of the pure formamide droplet.

4.3.2 Simulations of 10 nm NaI-formamide droplets

Having illustrated that the thermodynamics and phase behavior of a dielectric droplet can be changed and manipulated by external electric fields, we turn next to investigations of formamide droplets with a dissolved NaI salt at concentrations that are comparable with

those used in the experiments described in section 4.1. Simulations were performed on 10 nm NaI-formamide solutions with NaI/formamide ratios of 1/8 and 1/16, respectively in fields of 0.5, 0.625, 0.75, 1.0 and 1.5 V/nm. The concentrated droplets contain 7150 formamide molecules and 900 dissolved NaI units, corresponding to a 29% wt% solution that is nearly identical to the concentrated solution used in the experiments. The salt solution droplets were formed in the same manner as the pure formamide droplets described earlier.

Snapshots of the 1/16 salt solution droplet subjected to an electric field of 0.625 V/nm are shown in Fig. 6. A stage of initial elongation along the field direction is shown in Fig 6b, 400 ps after the field has been turned on. Fig. 6c, taken 300 ps later, exhibits further elongation of the droplet, and the onset of charge emission in the form of a Na^+ solvated ion. In the snapshot shown in Fig. 6d, which was recorded 1.1 nsec after the initial application of the field, formation of jets emanating from both ends of the elongated droplet are apparent. While a large solvated ion (with about 20 formamide ligands) with a single Na^+ ionic at the center is seen to be on the verge of being emitted at the positive end of the parent droplet (on the right in Fig. 6e), a large complex negative ion, $\text{I}(\text{NaI})(\text{NH}_2\text{CHO})_n$, is seen to be detaching at the other (negative) end of the droplet (left in Fig. 6e). About 25 ps after the instant when the configuration shown in Fig. 6d was recorded, a section of the material streaming from the positively charged side of the droplet thins down to a narrow hydrogen bonded filament of formamide molecules resulting in the detachment of a cluster, or nanodroplet, of charge +3 (see Fig. 6e) consisting of 17 Na^+ ions, 14 I^- ions and ~200 formamide molecules. This corresponds to a mass-to-charge ratio of about 3,700 Daltons.

The charged clusters that detach from the two ends of the droplet are accelerated by the applied electric field and their physical characteristics (charge, mass, size, energies), are recorded when they cross two planes (which we refer to as “detection planes”) located at ± 200 nm from the droplet center along the field direction (the z-axis). Properties of the recorded positively and negatively charged clusters are summarized in Fig. 7 as a function of the clusters’ radii, estimated by using or each cluster the equimolar radius defined by the cluster mass, m , the computed density of the NaI/formamide solution, $\rho \sim 1.32 \text{ g/cm}^3$, and the relation $m = 4/3\pi R^3\rho$. Figure 7a displays

the estimated surface electric field, E , of each cluster using Coulombs law (Eq. 2). A change in the dependence of E on the cluster radius R is observed at $R \approx 1$ nm, with cluster having radii $R \leq 1$ nm corresponding to single ions solvated by formamide molecules, while clusters with $R \geq 1$ nm are characterized as multi-ion droplets. In the latter dispersion forces may be expected to make a relatively, together with the electrostatic interactions. The change in behavior occurring for clusters with $R \geq 1$ nm is reflected also in the q/m and q/q_{Rayleigh} ratios plotted in Fig. 7b and 7c, respectively. The vertical dashed line in these figures corresponds to the experimental estimate (see Table 1) for the radius curvature of the electrospray, R_{max} , at the point of maximum electric field, E_{max} (see Eqs. 6 and 7). Essentially all the clusters recorded in the MD simulation have radii smaller than R_{max} . The few clusters with radii larger than R_{max} appeared at the very end of the simulation when breakup of the droplet into large fragments was observed. The experimental estimate for $E_{\text{max}} = 1.67$ V/nm (determined from Eqs. 6 and 7 as the average between the positive and negative polarities) is indicated by the thin solid line in Fig 7a. The estimated surface field of the simulated clusters remains very close to E_{max} for cluster radii in the droplet regime.

Figure 7b shows the charge-to-mass ratios for the clusters emitted by the simulated droplet. The mean value of the experimental q/m (Table 1) is shown as the horizontal dashed line. The MD values quickly approach the mean experimental value as the cluster sizes enter the droplet regime. If one uses E_{max} as a rough limiting value of the surface field for a charged droplet in Eq. (2) (Coulomb's law) to write $q=4\pi R^2 \epsilon_0 E_{\text{max}}$, an estimate for the upper bound of q/m can be obtained from:

$$q/m = 3\epsilon_0 E_{\text{max}} / \rho R. \quad (12)$$

The upper bound for q/m as a function of E_{max} and R is shown in Fig. 7b as a thin solid line. It is evident that the data for charged droplets ($R > 1$ nm) recorded in the MD simulations, follow this line.

Figure 7c shows the ratio between the observed (MD) charge and the predicted charge for Rayleigh instability and fission, computed from Eq. (1), where the surface tension $\gamma = 0.046$ N/m determined from the MD formamide droplet is used as an approximation for the salt solution. For clusters in the droplet regime, their charge

exhibits variations about 0.5 of the Rayleigh limit. Using Eq. (1) and (2) one obtains the upper limit for the ratio, $q/q_{Rayleigh}$:

$$q/q_{Rayleigh} = (\epsilon_0 R / 4\gamma)^{\frac{1}{2}} E_{\max}. \quad (13)$$

The corresponding values of Eq. (13) are shown as a solid line in Fig. 7c. This simple estimate captures the general trend and values observed in the MD simulation.

Fig. 8 compares profiles of ion and solvent molecule densities along the semi-major axis of the droplet spheroids for the cases shown in Figs. 6 (a-c). The figure also provides profiles of the local electric field and the charge, the latter given by the difference between positive and negative ion densities. The plotted electric field does not include the external field (0.625 V/nm). The densities are calculated by defining prolate spheroid shells that match the instantaneous droplet shape and end curvatures, and by counting the respective species between neighboring shells within a 1 nm core radius with respect to the z-axis. While the radial diameter of the narrowing droplet ends are less than that of the sampled core diameter (2 nm), the statistics of the density derive only from material inside the prolate spheroid shells, thereby yielding an accuracy superior to that obtained via simple binning of the z-axis. This process was not implemented for the case of the droplets in Figures 6d and 6e due to the narrow, rapidly varying, curvature. The data are obtained from 300 ps averages in the vicinity of the snapshots shown in Figs 6 (a-c).

The electric field strength along the z-axis is computed by binning, (during the simulation) the number of each species (Na, I, and 6 formamide atoms each having their own partial charge) with the z- and r- axis having bin widths of 0.2 nm. The binned data is averaged over a specified time in which the droplet does not change its shape or size significantly. Based on the charge of each species, the binned number of atoms provide the average amount of charge coming from each species in each of the radial 'rings' associated with each z-bin. The potential $V(Z)$ at a point, Z , on the z-axis is then a sum of the contributions from the total charge q_i in each of the binning rings of radius r_i for all the z-bins, (except for the central radial bin in the z-bin for which the field is determined):

$$V(Z) = \sum_i \frac{1}{4\pi\epsilon_0} \frac{q_i}{((z_i - Z)^2 + r_i^2)^{1/2}}, \quad (14)$$

The electric field at point Z without inclusion of the external field is then given by $E(Z) = -\partial V(Z)/\partial Z$.

The field-free droplet exhibits a depletion of ions at the interface, with a slightly higher ion density in the second or third interfacial layer (~ 6 Å from the interface) in comparison with the bulk. Differences between Na^+ and I^- densities are insignificant. This is consistent with the traditional view³⁵ pertaining to the behavior of the interfacial region of salt solutions, and it contrasts with recent MD and experimental findings in aqueous NaI solutions, where the highest I^- densities were found in the outer interfacial layer,^{35-38, 47, 49}; we defer further comments on this issue to the discussion section.

Figure 8b shows the profiles for the droplet shown in Fig. 6b. The interfacial charge density has clearly increased. In case of the positive end (right in Fig. 6), there is a slight preference for positive ions with ion densities of both polarities peaked at the interfacial layer. At the negative droplet end, there is a clear preference for negative ions in the interfacial layer. The electric field strength is highest beyond the droplet ends, with total fields (including the external field) exceeding 1.5 V/nm. Interestingly, the maxima are quite far from the ion density maxima, suggesting that the aligned dipoles of the solvent molecules contribute considerably to the field right outside the droplet. Indeed, when the field produced by the droplets is decomposed into contributions from the ions and the formamide molecules, we find that they each make a significant contribution. It is also of interest to note that the axial electric field of the pure formamide droplet (placed in an external field of 0.5 V/nm, see Fig 5) is essentially the same as that shown in Fig. 8b for the ionic solution droplet. In the pure formamide droplet the total contribution to the internal field comes from the aligned dipoles of the formamide molecules. From the fact that the internal fields are of similar values for the pure and the salt solutions drops, we conclude that the larger contribution of the molecular dipoles field in the pure drops reflects a higher degree of alignment in these drops compared to the salt solution drops where the dissolved ions frustrate the molecular

alignment in the field direction. Direct analysis of the dipole alignments in pure formamide and salt solution drops verifies the above conclusion. We also note that the external field strengths of the order of V/nm originating from droplet polarization are established very shortly subsequent to application of the external and before the occurrence of any significant field-induced elongation.

The field produced by the droplet vanishes asymptotically far from the droplet so that the total summed field converges to the external constant field of 0.625 V/nm. The negative field inside the droplet is of the same nature as the field within a dielectric slab or sphere subjected to an external field. Charges of opposite polarity are induced on opposing sides of the dielectric and this creates an internal field that opposes the external field.

In the present case, the average internally induced field is ~ -0.58 V/nm, corresponding to a small total internal field, $E = 0.625 - 0.58 \sim 0.04$ V/nm. Such small internal fields are typical of dielectric materials responding to external electric fields. The high sensitivity of computed dielectric properties to small variations in this internal field necessitates the accumulation of sufficient data that would permit meaningful statistical analysis. The highly oscillatory nature of the field within the drop seen in our simulations, is due to limited statistics and the fact that the computed field reflects a non-uniformity of the ionic distribution that does not self-average over the averaging interval of ~ 300 ps used in these simulations.

4.3.3 Charge emission statistics

Statistics on charge emission is gathered by recording the passage of all ejected clusters through the aforementioned “detection planes” placed at ± 200 nm along the z-axis. The atomic position and momentum data of each cluster is also recorded so that the evolution of an individual cluster can be examined in a separate continued simulation of the isolated species.

The surface tension of the NaI-formamide droplets is comparable to that of the pure formamide droplet and the predicted critical field for instability²⁵ discussed earlier (see also Fig. 5) is similar. However, in the salt-solution case, the droplet does not simply elongate to another stable configuration at the critical field. Instead the imbalance

between electrical stresses and capillary forces is relieved through a more favorable route, namely one involving formation of a jet of charged clusters (at each of the elongated nano-drop). At the smaller investigated fields (< 1 V/nm), the droplets elongate more slowly and emit cluster ions less frequently with the result that capillary, Rayleigh-type, instabilities lead to break-up of the droplet into large charged segments that are accelerated out of the computational cell before the number of cluster ions that are emitted are adequate for meaningful statistics. Consequently, when investigating cluster-ion emission statistics we focus on simulations of drops at the higher field strengths. The improved statistics associated with the higher charge fluxes provide a better comparison with the mass spectrometric measurements.

Under the influence of an electric field of 1.5 V/nm, the droplet begins to deform about 10 to 20 ps prior to charge emission, along the axial field direction, of positively and negatively charged solvated ions from opposite ends of the drop. Over the course of about 1 ns, the parent drop continues to elongate to at most an aspect ratio $\eta = 8$, and the onset of charge emission is observed. The continuous stream of charged particles prevents elongation to higher aspect ratios such as the one observed for the pure formamide droplet (see Fig. 5). The simulations demonstrate that charge emission happens from multiple sites on each end of the drop. This is consistent with a stressed, multi-cone electrospray regime discussed earlier. We remark here that because of the early emission of charged particles in simulations employing a high electric field, (1.5 V/nm) we focused on lower applied fields which enable comparisons with the experiments, particularly of issues pertaining to the dynamics of the particle emission and droplet formation.

The charge distribution of cluster ions originating from formamide droplets containing 29 % (by weight) of dissolved NaI is shown in Fig. 9. Results are presented here for two separate simulations having externally applied electric field strengths of 1.0 and 1.5 V/nm. The abundances of charge of both these studies are similar showing that most of the observed clusters have charge ± 1 , however, multiply charged species are also observed.

A more detailed information on the ionic composition of the most frequently observed clusters of charge ± 1 is shown in Fig. 10. In case of singly positively charged

clusters, the fraction of clusters with ionic composition Na^+ , Na_2^+I^- , etc. and for negatively charged clusters, the fraction corresponding to I^- , Na^+I_2^- , etc. are shown without regard to the number of accompanying adsorbed formamide molecules. While multi-ion clusters contribute, the primary contribution is from single-ion clusters (Na^+ and I^- with varying numbers of adsorbed formamide molecules). Furthermore, the multi-ion cluster fraction increases with field. This is consistent with the present experimental single cone-jet observations at lower representative field strengths, where the multi-ion fraction due to Na_2^+I^- and Na^+I_2^- solvated ions, is very small (see Fig. 3 and Tables. 1-4).

In Fig. 11 we compare the solvation number distribution of the singly-charged positive and negative cluster ions compiled from the concentrated, 1.5 V/nm MD simulation to those observed in the concentrated electrospray experiment. Also shown are MD results adjusted for a ~ 30 μs flight time using the calculated survival fractions from Tables 7 and 8 for 300K. For Na^+ and I^- solvation numbers exceeding 6 and 5, respectively, a zero survival fraction is assumed, while for $n < 4$ and 3, respectively, a 100 percent survival is implied. The Na^+ clusters have predominantly 4-5 formamides, and the adjusted cluster distribution compares well to the experimental abundances. The I^- clusters exhibit a much broader distribution with a bias toward lower solvation numbers. The adjusted MD statistics are again consistent with the experimental results (Tables 2 and 3) for a single cone-jet electrospray of the same concentrated solution.

5. Discussion

The close correspondence that we found between the data measured in the vacuum electrospray experiments and the results recorded in our theoretical MD simulations performed on liquid drops (made of pure formamide or NaI/formamide solutions), demonstrate that such coordinated, complementary, and supplementary studies are most valuable sources of information and deep insights pertaining to the physics and operational control of electrospray, nanojets, and charged droplets under the influence of high electric fields. Having presented in the previous sections our laboratory measurements and theoretical simulations we discuss now certain issues that emerged through the analysis of the results of our investigations.

The characteristic parameters of our experiments (see Table 1) demonstrate that the cone-jet generated in these experiments operates in the nanoscale jet regime with sufficiently high fields generated normal to the liquid surface to induce field evaporation of ions. The observed average mass-to-charge ratios and the significant cluster-ion currents are signatures of a mixed droplet/ion emission regime. The presence of field-induced ion evaporation is consistent with the estimated values for the maximum surface-normal fields E_{max} (between 1.4 and 1.7 V/nm) and for the critical radii, R_{max} (between 2 and 3 nm) derived from the axial emission currents and mass flows, thus confirms predictions obtained from the theory of cone-jet emission.¹⁵⁻²² The derived jet diameter of about 5 nm is comparable to that of the simulated droplet, supporting the comparison between the present electrospray experiment and the MD droplet simulations.

Decreasing the salt concentration of the NaI/formamide solution leads to a reduction of the maximum surface-normal field strength and an increase of the associated radius of curvature. This is consistent with Eqs. (6) and (7). The expected increase in m/q , however, is found to be significant only for negatively charged emitted particles. This somewhat surprising result can be explained by the substantial decrease in charged particle beam divergence upon dilution, as reflected by the ratio of the Faraday Cup current with respect to the total emitted current. As angular distribution measurements on ionic liquid cone-jets operated in a nano regime have shown,^{32, 33} the m/q distribution can be non-uniform with respect to the emission polar angle. Thus, the derived average m/q value is only representative of charge emission captured at small angles with respect to the capillary axis. The non-uniformity reported by Chiu et al. for the ionic liquid, [Emim][Im],^{32, 33} is consistent with predictions that the surface electric field is highest at the cone-jet neck, where field-evaporated ions are driven away from the cone-jet axis.^{22, 24} The respective field-evaporated ions are, therefore, preferably emitted at large angles while droplets, emitted from the jet tip, have narrow angular distributions centered on axis. This interpretation was further confirmed for the ionic liquid by the measured energy distributions demonstrating that the ions peak at energies nearly equal to the emitter potential, while the droplets appear at lower potentials. Consequently, if similar field evaporation dynamics apply in the present concentrated NaI/formamide solution, a significant fraction of the ion current is not detected by the Faraday Cup, and the average

m/q of the entire jet is considerably higher for cases with substantial divergence of the ionic component in comparison with the droplet component. This interpretation, however, is contradicted by the fact that the present retardation potential measurements (Fig. 4) show that only a small fraction of ions are produced at energies exceeding the droplet energy, suggesting that most ions are formed in a region of the neck downstream from where ohmic losses have occurred. Similar retarding potential results have been derived by Gamero-Castaño for concentrated NaI/formamide at low flow rates.²⁴ Consequently, the field evaporation dynamics of the present solution may not be equivalent to that observed for the ionic liquid [Emim][Im]. This does not discount the possibility that ion emission is more divergent than the droplet spray.

In addition to field evaporation from the jet, ions can be emitted from droplets as described by the mechanism of Iribarne and Thomson⁶ for electrosprays of volatile solvents in an ambient atmosphere. This requires that the surface electric field strength, given by Eq. (2), exceeds the ion evaporation limit. However, as pointed out by Gamero-Castaño and Fernández de la Mora,²² this mechanism can only lead to a current that is a small fraction of the total droplet current because of the fast decrease of the electric field in the direction normal to the liquid surface following the emission of ions.

Further insights were obtained through comparative mass spectrometric studies of concentrated and dilute NaI/formamide solutions. While the distribution of Na^+ solvated ions is very similar at the two concentrations, apart from a greater number of trace ions at high solvation numbers, the I^- solvated ion distribution broadens considerably and shifts to higher solvation numbers upon dilution. This behavior is consistent with recent theoretical and experimental investigations of aqueous salt solutions,^{34-40, 43-49} where a preference at the interface for more polarizable anions such as I^- was explained in part with the broader range of solvation numbers that the anion can accommodate in comparison with less polarizable anions and cations, which prefer more rigid, hydrogen-bonded solvation shells. Thus, as the concentration decreases, more solvent molecules are available to bond with I^- , while Na^+ maintains a tightly bound structured solvation shell.

The Na^+ solvation number (the number of solvating formamide (FA) molecules per solvated Na^+ , $\text{Na}^+(\text{FA})_n$) drops rapidly for solvated ions with $n > 4$, for which room

temperature thermal instability is predicted. However, an increased number of ions with high, thermally unstable, solvation numbers is observed upon dilution. This suggests that a significant number of cluster ions are emitted with large, unstable, solvation numbers, and subsequently they lose (via evaporation) some of the solvating ligands, resulting in evaporative cooling of the product cluster ions. This effect is even more extreme for the I^- cluster ions to the point that the most abundant solvation number lies beyond the present predictions of thermal stability at a liquid temperature of 298 K (Table. 6).

Similar behavior was observed in our experiments on KI solutions, where the K^+ solvated ions also have maximum abundances near the predicted limit of thermal stability. The main difference between the KI and NaI solutions are the survival, in the KI case, of complex ions (of both polarities) upon dilution for both ion polarities. The KI experiments were mired by crystallization of the solute and, therefore, had to be conducted at significantly lower molar concentrations. The higher propensity for forming complex ions, $X^\pm(KI)(HCONH_2)_m$, despite the lower concentration in comparison with the NaI solution, may be a manifestation of the lower solubility of the KI solute.

The snapshots of the drop configurations recorded in the simulation of a NaI/Formamide solution droplet with a (NaI):16 (formamide) ratio, under the influence of an electric field of 0.625 V/nm, reveal a number of features that are in direct correspondence with the experimental observations. In particular, in both cases we observe mixed droplet formation and field ion evaporation events. Formation of nanojets is clearly observed in the simulations (See Fig. 6d where a jet with a diameter of about 2nm is shown). However, we remark that the jet emerging in our simulation is a transient state whose further development prior to particle emission and breakup into droplets may be limited by the finite size of the simulated drop. In the experiment, on the other hand, a continuous (unlimited) source of liquid is present, thus allowing the development of steady state jet (flow) conditions. Therefore, in order to allow detailed theoretical study of the breakup processes it is desirable to slow down the breakup processes. To this aim we used MD drop simulations performed with lower applied electric fields. Interestingly, in the simulations the majority of cluster ions are found to be emitted from the tip of the jet rather than from the neck region next to the Taylor cone (see Fig. 1). This finding is consistent with the experimental energy distributions of solvated ions that demonstrates

that indeed most ions are emitted closer to the jet region, that is, beyond the cone-neck region where ohmic losses occur. This observation, contrasts continuum electrohydrodynamic theory predictions of maximum surface electric field strengths at the neck.^{22, 24}

Because of the small dimensions of the jets formed in the MD simulations, and deduced from analysis of the experimental measurements, one may indeed expect that a continuum approach would fail to provide an adequate description of the evolution and breakup processes of the complex liquid system on which we focus here. From inspection of the drop configurations displayed in Fig. 6 we observe the occurrence of spatial and temporal fluctuations of the ion density that are expected to influence in a significant manner the electric field distribution and the consequent stability and evaporation/fragmentation dynamics of the system under study. Indeed, we have noted that droplet formation events (location and timing) correlate with instances of ion bunching in the jet region. These observations are likely to be of particular relevance to ionic solutions where bunching of the solute ions (sodium and iodine ions in our case) occurs; indeed, in the case of an ionic liquid (where more uniform ion distributions are expected) characteristics that indicate emission from the neck region have been observed,^{32, 33} even though the jet diameter in that system is estimated to be similar to that found by us in the present study.

Additionally, stochastic thermal effects play a much increased role for fluid jets of nano-scale dimensions,⁵¹ modifying the kinetics of fluid pinch-off from the predictions of a purely deterministic continuum approach.

An important prediction obtained from the MD simulations concerns a crossover as a function of the size of the emitted species, that distinguishes between solvated single-ion clusters with radii $R \leq 1$ nm, and multi-ion droplets that emerge for larger size fragments, $R > 1$ nm. Such crossover is indeed found experimentally, and it may be explained through electrostatic considerations (see Fig. 7). This crossover reflects stronger bonding in the smaller, single-ion solvated clusters due to direct ion-dipole interactions which correlate with the ability to sustain larger values of charge-to-mass ratios compared to larger size clusters (see Fig. 7b).

Emission of clusters that include ion pairs was detected in both the experiments and simulations. While only species containing a single ion pair were observed in the experiments for concentrated NaI formamide solutions, and none for the dilute solution, higher fractions of such ions with species containing 2 and more ion pairs were found in the simulation (Fig. 10). Note that the respective radii of the complex ions containing ion pairs exceed 1 nm, and exhibit electrostatic properties of droplets according to the analysis of Fig. 7. We have not conducted an RRKM analysis and thermo-chemical analysis for these species to assess whether such complex ions decay faster than the experimental time scale. Similarly, no multiply charged ions were detected in the experiments, while they were found in the simulation (Fig. 9). Higher field-strengths do not appear to be the source of these findings since an increase of the field in the simulations from 1 V/nm to 1.5 V/nm did not affect the observed trends (see Figures 9 and 10). We note however, it can be said that earlier vacuum electrospray studies conducted with glycerol solutions observed a multitude of solvated ions including metastable ions and multiply charged species.^{2, 12, 13, 85}

In general the emitted cluster ions recorded in the MD simulations contain more nascent formamide molecules (that is they are characterized by larger solvation numbers) than the clusters observed in the experiments where typical flight times (that is, the elapsed time between the instant of cluster generation and the moment of it's detection) are of the order of 30 μ sec. The recorded occurrence of larger solvated ion clusters is likely to be correlated with the propensity of the solvent (formamide) to form hydrogen bonds (see Figs. 6(c-e)). Since the largest solvated ions observed in the MD simulation are thermally unstable, evaporative loss of formamide molecules over longer flight times can effectively lower the average solvation numbers to values close to those found experimentally (see Fig. 11). The observation of larger solvated ions in the simulations suggests that such larger clusters ions are indeed generated in the laboratory experiment, and that subsequently these large, thermally (room temperature) unstable, clusters reduce their size via a cascades of evaporative cooling processes that occur along the clusters' trajectories to the detector. Indeed, separate simulations on large thermally unstable cluster ions show that the loss of a formamide molecule leads to an approximate reduction in cluster-ion temperature of 50 K. As evident from the data shown in Table 7,

a 50 K change in temperature has a rather significant effect on the stability of the cluster ions. We remark here that

the MD simulation was conducted at a relatively high external field, corresponding to stressed conditions, which could explain the increase of the nascent cluster-ion temperature from 310 K to about 400 K from the beginning to the end of the simulation. While the comparison with the present experimental solvated Na^+ ion distributions, predicted thermal stabilities, and RRKM decay rates suggest a surface temperature below 350 K, a 200V drop between the capillary potential and the observed ion appearance potential indicates the occurrence of ohmic heating in the neck region of the cone-jet. Thus, a slightly elevated temperature at the point of ion field evaporation could be expected.

A rather convincing illustration that the emitted charged droplets recorded in the simulations are consistent with the values deduced from the experimental data for the characteristic maximal electric field, E_{max} , and the corresponding local curvature (determined by the local radius, R_{max} , of the flowing fluid structure), can be found in Fig.7. Except for droplets emitted at the very end of the simulation, where the main droplet disintegrates, the radii of all the emitted droplets are found to be smaller than the polarity averaged experimentally determined value of R_{max} . We also find that, coincident with the above, the surface fields of the droplets are close to the experimental, polarity averaged, value of E_{max} , which is found to be close in value to the interfacial field determined from the simulations (see Figs. 8b and 8c). Additionally, the charge-to-mass ratio associated with the experimental maximal value of the electric field, E_{max} (Eq. 12), is found to agree well with the values derived for the emitted charged droplets. Finally, the observation that the emitted droplets are charged to within 0.4 to 0.5 of the Rayleigh limit is found to be consistent with Eq. (13) when using the experimental value of E_{max} .

It is pertinent to remark here on the small asymmetry between the calculated negative and positive ion interfacial density profiles (see Fig. 8), particularly in light of recent interest in the interfacial properties of aqueous solutions.³⁴⁻⁴⁹ Upon application of an electric field the ion density at the interface increases (see Fig. 8b). While at field-free conditions no discernable difference is found between the negative and positive ion interfacial densities, a simulated drop placed in a uniform electric field exhibits a small

preference for negative ions near the negative polarity interface, while positive ions are only marginally preferred at the positive end. The derived solution-induced electric field strength normal to the surface at the negative end exceeds 1.0 V/nm, corresponding to a total field strength of about 1.6 V/nm when including the external field. This value is again in excellent agreement with the derived values for the concentrated solution (see value in Table 1, obtained with the use of Eq. (6)). The field is slightly lower at the positive end. The large surface fields at the polar ends of the drop are not solely a reflection of the ionic charge density, but are attributable to both aligned formamide dipoles as well as field-induced polarization and separation of the ionic charges. Similar surface fields are deduced for the pure formamide droplet (see Fig. 5) where the absent contribution to the field coming (in the case of salt solution) from the solvated ions is compensated by an increased field due to a higher formamide dipole-field alignment. As aforementioned, the above indicates that in solution drops the presence of solvated ions frustrates the alignment of the dipolar solvent molecules.

The observed preference of negative ions at the interface under the influence of an external electric field is not as pronounced as the corresponding findings at aqueous interfaces under field-free conditions, where large polarizable anions were particularly preferred over cations in the interface layer.^{37, 38} In the present simulations the anions (I^-) are treated as a point charge, and it is possible that the inclusion of a polarization term in the interaction potential may enhance the anionic presence; indeed the role of the anionic polarization term has been discussed in the context of MD simulations of aqueous solutions.^{38, 41, 42} From the fact that the simulated field-free NaI/formamide droplet exhibits no difference between anionic and cationic densities in the interface layer (where ion depletion occurs as expected from a solvation energy consideration), we conclude that the minor preference for the anions to reside in the interfacial layer, found in simulations under the effect of an external field, is related to the interaction of the ions in the cluster with the applied field. Because the solvation number distributions are broader for the larger anions, and because the ligand binding energies are weaker (see Table 6), it may be expected that the propensity of the formamide molecules coordinated with the I^- to align with the field is higher than that of molecules coordinated with the Na^+ cations, resulting in a stronger attraction towards the high-field region at the interface. The lack

of a charge preference in the field-free NaI/formamide droplet could also be attributed to the nanometer-scale droplet confinement effects, surface curvature, and characteristics of the liquid solvent (that is, formamide in the present simulations versus water in previous interfacial studies). The chemical identity factor could be of principal significance, particularly in light of the fact that the behavior of aqueous solutions is often discussed in terms of hydrogen bonding between water molecules in clusters of large anions, versus symmetric solvation in the case of the cationic systems.³⁵ Accordingly, it has been shown through MD simulations of aqueous Na^+ and Cl^- clusters, that Na^+ is solvated symmetrically in the center of the clusters, while Cl^- resides on the surface of a water cluster.⁸³ This was confirmed experimentally for the larger halide ions in water dimer clusters by Johnson and coworkers.⁸⁴ The present *ab initio* optimized structures of formamide-solvated ions, however, show no evidence for hydrogen bonding with both the formamide-solvated Na^+ and I^- ions located close to the centers of the corresponding clusters.

6. Summary

In this paper we presented laboratory experiments and theoretical investigations aiming at characterizing and understanding the atomic-scale structure, energetics, stability, dynamics, and fragmentation processes of complex liquids under the influence of high electric fields. The present MD simulations of drops of NaI/formamide solutions placed in a uniform field reproduce faithfully the main salient experimental features observed in vacuum electrospray ionization experiments of solutions of similar concentration, operated in a single cone-jet mode with jet dimensions comparable to the drop size. At these conditions, Taylor cones spray charged particles in a mixed solvated ion/droplet regime. The MD simulation of a droplet subjected to a uniform electric field of 0.625 V/nm shows the occurrence of droplet fission and field ion evaporation processes. The simulation predicts that ion emission occurs at the tip of the jet that develops beyond the neck connecting to the Taylor cone (see Figs.1, 6d and 6e). This contrasts with continuum electrohydrodynamic theory where emission from the neck region is predicted.^{22, 24} The results from the simulation are consistent with the present experimental findings that most of the field evaporated ions are formed with energies

near, or lower, than those of the charged droplets. The surface normal field strength determined from the simulation near the point of charge emission (for the concentrated solution drop) is determined to be ~ 1.6 V/nm, in excellent agreement with the field derived from the experimental observations using continuum electrostatic theory. The size dependence of the surface electric field and charge-to-mass ratios of droplets emitted in the MD simulation are fully consistent with the experimentally derived maximum surface field strength and associated curvature. A transition in the electrostatic properties of the emitted clusters as a function of size is observed at radii of ~ 1 nm, corresponding to a transition between solvated single ions (for $R \leq 1$ nm) and multi-ion droplets (for $R > 1$ nm). This crossover is attributed to the stronger intermolecular forces and the consequently higher sustainable charge densities in the solvated single ions.

The simulated and measured solvation number distributions for $\text{Na}^+(\text{HCONH}_2)_n$ and $\text{I}^-(\text{HCONH}_2)_n$ are in good agreement. While the Na^+ cluster-ion distributions are governed primarily by thermal stability and are independent of concentration, the I^- cluster-ion distributions broaden with dilution. Similar behaviour is observed experimentally with KI/formamide solutions. Larger cluster ions that are thermally unstable at 300 K are observed and attributed to evaporatively cooled species. Complex ions including ion pairs are observed both experimentally and in the simulations. While multiply charged ions are not observed experimentally, minor quantities of multiply charged ions survive the ~ 15 ps flight time of the simulation space.

The present MD simulations reveal that for a NaI/formamide droplet at field-free conditions, ion densities are depleted in the interfacial layer and that there is no preference of anions over cations. Upon application of a field, ion densities in the interfacial layer increase at locations where the surface field strength is high. A slight preference for anions is observed at the negative droplet end following field deformation. This is attributed to weaker solvent molecule bonding to I^- in comparison to Na^+ , as determined by the present *ab initio* calculations, and the resulting higher degree of alignment of the formamide dipole in the vicinity of the anion.

Table 1. Electrospray source parameters of the experimentally investigated NaI/formamide solutions. $I(\text{tot})$ and $I(\text{Faraday Cup})$ correspond to the total emission and Faraday Cup currents, respectively. \dot{m} (QCM) (ng s^{-1}) is the mass flow as measured on the QCM. E_{max} and R_{max} correspond to the maximum electric field strength and the associated radius of curvature at the jet neck given by Eqs. (6) and (7).

NaI mole ratio	1:8.4		1:36.9	
Conductivity	1.64 S/m		1.26 S/m	
Extraction Voltage (V)	2,000	2,000	2,400	2,400
Polarity	+	-	+	-
$I(\text{total})$ (nA)	250	464	120	200
$I(\text{Faraday Cup})$ (nA)	28	58	63	60
\dot{m} (QCM) (ng s^{-1})	2.4	3.0	5.4	4.0
m/q (Daltons)	8,410	4,930	8,330	6,360
E_{max} (V/nm)	1.70	1.64	1.42	1.49
R_{max} (nm)	2.30	2.48	3.29	2.98

Table. 2. Mass distributions for $\text{Na}^+(\text{HCONH}_2)_n$ and $\text{Na}^+(\text{NaI})(\text{HCONH}_2)_m$ ions sprayed from concentrated and dilute (1:8.4 and 1:36.9 NaI-formamide mole ratios, respectively) NaI/formamide solutions. I is the recorded normalized mass spectral intensity.

I			I	
n	Concentrated	Dilute	m	Concentrated
1	0.0018	0.0007	0	0.0012
2	0.0139	0.0111	1	0.0033
3	0.1437	0.0967	2	0.0016
4	0.5467	0.4674	3	0.0024
5	0.1751	0.1505	4	0.0078
6	0.0479	0.0699	5	0.0155
7	0.0195	0.0418	6	0.0030
8	0.0090	0.0335	7	0.0012
9	0.0024	0.0240	8	0.0012
10	0.0009	0.0169	9	0.0014
11	0.0002	0.0148		
12	0.0004	0.0128		
13		0.0148		
14		0.0158		
15		0.0123		
16		0.0169		

Table. 3. Mass distributions for $\Gamma(\text{HCONH}_2)_n$ and $\Gamma(\text{NaI})(\text{HCONH}_2)_m$ ions sprayed from concentrated and dilute (1:8.4 and 1:36.9 NaI-formamide mole ratios, respectively) NaI/formamide solutions. I is the recorded normalized mass spectral intensity.

n	I		m	I	
	Concentrated	Diluted		Concentrated	
0	0.0281	0.0350	0	0.0073	
1	0.2151	0.0817	1	0.0141	
2	0.2949	0.0682	2	0.0460	
3	0.1855	0.1051	3	0.0457	
4	0.1011	0.1276	4	0.0221	
5	0.0402	0.1547			
6		0.0846			
7		0.0570			
8		0.0692			
9		0.0492			
10		0.0399			
11		0.0501			
12		0.0292			
13		0.0317			
14		0.0169			

Table. 4. Mass distributions for $K^+(HCONH_2)_n$ and $K^+(KI)(HCONH_2)_m$ ions sprayed from concentrated and dilute (1:41 and 1:83 KI-formamide mole ratios, respectively) KI/formamide solutions. I is the recorded normalized mass spectral intensity. Trace amounts of unidentified peaks are not included.

n	I		m	I	
	1/4 volumetric diluted	1/8 volumetric diluted		1/4 volumetric diluted	1/8 volumetric diluted
0	0.0115	0.0050	0	0.0111	0.0277
1	0.0031	0.0009	1	0.0107	0.0219
2	0.0085	0.0060	2	0.0051	0.0104
3	0.0106	0.0421	3	0.0018	0.0037
4	0.0861	0.1745	4	0.0010	0.0017
5	0.1510	0.1758	5	0.0010	0.0018
6	0.1368	0.0827	6	0.0008	0.0016
7	0.1091	0.0576	7	0.0010	
8	0.0959	0.0476			
9	0.0684	0.0385			
10	0.0497	0.0330			
11	0.0446	0.0415			
12	0.0462	0.0377			
13	0.0416	0.0429			
14	0.0336	0.0374			
15	0.0248	0.0449			
16	0.0334	0.0405			

Table. 5. Mass distributions for $\Gamma(\text{HCONH}_2)_n$ and $\Gamma(\text{KI})(\text{HCONH}_2)_m$ ions sprayed from concentrated and dilute (1:41 and 1:83 KI-formamide mole ratios, respectively) KI/formamide solutions. I is the recorded normalized mass spectral intensity. Trace amounts of unidentified peaks are not included.

n	I		m	I	
	1/4 diluted	1/8 diluted		1/4 diluted	1/8 diluted
0	0.0076	0.0059	0	0.0018	0.0004
1	0.0095	0.0142	1	0.0029	0.0003
2	0.0444	0.0664	2	0.0057	0.0117
3	0.1608	0.0772	3	0.0183	0.0280
4	0.2465	0.0839	4	0.0236	0.0309
5	0.2032	0.1305	5	0.0164	0.0298
6	0.0453	0.1072	6	0.0067	0.0367
7	0.0433	0.0569	7		0.0241
8	0.0392	0.0616	8		0.0152
9	0.0253	0.0416	9		0.0176
10	0.0206	0.0303	10		0.0157
11	0.0294	0.0383			
12	0.0263	0.0198			
13		0.0228			
14		0.0185			

Table. 6. Thermochemistry of $\text{Na}^+(\text{NH}_2\text{CHO})_n$, $n = 1-6$, $\text{K}^+(\text{NH}_2\text{CHO})_n$, $n = 1-6$, and $\Gamma(\text{NH}_2\text{CHO})_n$, $n = 1-5$ solvated ions determined with the indicated *ab initio* methods. The internal energy, E_{int} , signifies the 298.15 K thermal energy above the zero-point energy, E_{zpe} . The binding energy, $D(\text{MF}_{n-1}-\text{F})$, refers to the loss of a single solvent molecule, $\text{F}=\text{HCONH}_2$. Also shown are thermochemical data at 310 K determined for the “classical” clusters bound by the MD simulation inter-atomic potentials. All values are given in kcal/mol.

	Quantum Chemistry			MD	
	E_{zpe}	E_{int}	$D(\text{MF}_{n-1}-\text{F})$	E_{int}	$D(\text{MF}_{n-1}-\text{F})$
$\text{Na}^+(\text{NH}_2\text{CHO})_n$			B3LYP/6-31G(d)		
1	30.1	3.33	39.7	1.84	21.6
2	59.9	6.71	33.3	3.69	19.8
3	89.4	10.3	24.1	5.53	16.8
4	118.4	14.0	17.2	7.40	14.3
5	149.5	16.3	15.7	9.24	11.3
6	178.2	20.2	7.2	11.1	9.57
$\text{K}^+(\text{NH}_2\text{CHO})_n$			B3LYP/6-31G(d)		
1	29.8	3.46	28.7		
2	59.3	7.02	24.0		
3	88.7	10.6	19.5		
4	117.7	14.4	15.6		
5	148.8	16.8	14.4		
6	178.3	20.3	10.8		
$\Gamma(\text{NH}_2\text{CHO})_n$			MP2/6-311G+(d,p)/6-311+G(df)		
1	27.8	3.6	17.4	1.85	13.1
2	56.0	7.0	14.9	3.70	12.9
3	83.7	10.8	12.1	5.54	11.3
4	111.8	14.3	10.9	7.39	10.2
5	140.0	17.1	8.4	9.24	8.6

Table. 7. Survival fractions for selected $\text{Na}^+(\text{NH}_2\text{CHO})_n$ ions evaporated with characteristic temperatures of 300, 350 and 400 K. The survival fractions are listed for infinite observation times, t , flight times through mass spectrometric experiment (MS), and the MD simulation period (MD).

t	n	4	5	6
$T = 300 \text{ K}$				
∞		0.927	0.503	8.0×10^{-5}
MS (26, 28, 31 μs)		0.994	0.662	1.0×10^{-4}
MD (15 ps)		1.000	0.903	7.2×10^{-3}
$T = 350 \text{ K}$				
∞		0.702	0.148	0.000
MS (26, 28, 31 μs)		0.920	0.279	0.000
MD (15 ps)		1.000	0.601	8.0×10^{-4}
$T = 400 \text{ K}$				
∞		0.332	0.035	0.000
MS (26, 28, 31 μs)		0.718	0.070	0.000
MD (15 ps)		1.0	0.273	0.000

Table. 8. Survival fractions for selected $\Gamma(\text{HCONH}_2)_n$ ions evaporated with characteristic temperatures of 300, 350 and 400 K. The survival fractions are listed for infinite observation times, t , flight times through mass spectrometric experiment (MS), and the MD simulation period (MD).

t	n	3	4	5
$T = 300 \text{ K}$				
∞		0.859	0.295	0.036
MS (29, 32, 34 μs)		0.957	0.548	0.091
MD (15 ps)		1.000	0.974	0.407
$T = 350 \text{ K}$				
∞		0.620	0.088	0.006
MS (29, 32, 34 μs)		0.811	0.224	0.016
MD (15 ps)		1.000	0.837	0.121
$T = 400 \text{ K}$				
∞		0.341	0.023	0.000
MS (29, 32, 34 μs)		0.570	0.067	0.001
MD (15 ps)		1.0	0.560	0.024

Figure Caption:

Fig.1. Schematic representation of an electrospray cone-jet.

Fig. 2. Schematic diagram of the mass spectrometric experiment.

Fig. 3. Sample positive and negative ion mass spectra of the concentrated (28.4% wt.) NaI-formamide solution. Solvated ion solvation number assignments are shown.

Fig. 4. Retarding potential measurements of solvated ion and droplet (corresponding to high pass, $m/q > 400$) energy distributions. The capillary potential was biased at 550 V, and the analyzer was at ground.

Fig. 5. MD simulation of a 10 nm formamide droplet prior to and after the application of an electric field. When a critical field is exceeded, the droplet lengthens to another stable configuration. The calculated critical field for a 10 nm droplet assumes a surface tension of 0.046 N/m. The aspect ratios, η , for the various configurations are specified in the figure.

Fig. 6. MD simulation snapshots of a 10 nm diameter droplet of a 1:16 ratio NaI/Formamide solution during different stages of elongation due to the application of a uniform external electric field of 0.625 V/nm. Na^+ and I^- are shown as red and yellow spheres respectively. Time with respect to field application: a) 0 ps; b) 400 ps; c) 700 ps; d) 1,100 ps; e) 1,125 ps. The aspect ratios, η , for the various configurations are specified in the figure.

Fig. 7. Properties of the charged clusters emitted from the droplet described in Fig. 5 as a function of cluster radius: (a) the estimated electric field at the droplet surface, (b) the charge to mass ratios and (c) the observed (MD) charge divided by the predicted charge for Rayleigh instability and fission. The added dashed and thin solid lines compare MD results to estimates based on the experimental electrospray results (from Table 1, see text for details).

Fig. 8. Number densities and induced electric field of the 1:16 ratio NaI/Formamide droplet along the field direction for (a) no external field, (b) elongating in constant external 0.625 V/nm field before emitting ions and (c) during the time of initial cluster-ion emissions. The profiles correspond to the respective snapshots in Fig. 5a-c. The droplet components are designated as in (a) while the relative densities of Na to I and the electric field are as given in (b) and (c). The internal field of the droplet (generated by induced surface charges) is shown as lighter lines and fluctuates around ~ -0.6 V/nm. The aspect ratios, η , for the various configurations are specified in the figure.

Fig. 9 Charge abundances of ion-containing clusters emitted from a 1:8 ratio NaI/Formamide droplet (29% by weight of dissolved NaI) placed in a uniform external field. Results are shown for two simulations having external field strengths of 1.0 and 1.5 V/nm. The observation occurred at ± 200 nm from the droplet.

Fig. 10. Ion composition of singly charged formamide/NaI clusters emitted from a 1:8 ratio NaI/Formamide droplet (29% by weight of dissolved NaI) placed in a uniform external field strengths of 1.5 V/nm (top) and 1.0 V/nm (bottom). The observation occurred at ± 200 nm from the droplet.

Fig. 11. Solvation number distribution of single-ion clusters emitted from a 1:8 ratio NaI/Formamide droplet (29% by weight of dissolved NaI) placed in a uniform external field of 1.5 V/nm. The observation occurred at ± 200 nm from the droplet. MD results are compared with experiment. MD results corrected for 30 μ s flight time (adjusted MD) are also shown (see text for details).

REFERENCES

1. J. B. Fenn, M. Mann, C. K. Meng, S. F. Wong and C. M. Whitehouse, *Science*, 1989, **246**, 64.
2. M. N. Huberman and S. G. Rosen, *J. Spacecraft*, 1974, **11**, 475-480.
3. D. H. Reneker and I. Chun, *Nanotechnology*, 1996, **7**, 216-223.
4. L. Rayleigh, *Phil. Mag*, 1882, **14**, 184-186.
5. M. Dole, L. L. Mack, R. L. Hines, R. C. Mobley, L. P. Ferguson and M. B. Alice, *J. Chem. Phys.*, 1968, **49**, 2240-2249.
6. J. V. Iribarne and B. A. Thomson, *J. Chem. Phys.*, 1976, **64**, 2287-2294.
7. B. A. Thomson and J. V. Iribarne, *J. Chem. Phys.*, 1979, **71**, 4451-4463.
8. I. G. Loscertales and J. Fernández de la Mora, *J. Chem. Phys.*, 1995, **103**, 5041-5060.
9. V. Katta, A. L. Rockwood and M. L. Vestal, *Int. J. of Mass Spectrometry and Ion Processes*, 1991, **103**, 129-148.
10. J. B. Fenn, J. Rosell and C. K. Meng, *J. Am. Soc. Mass Spectrom.*, 1997, **8**, 1147-1157.
11. P. D. Prewett and G. L. R. Mair, *Focused ion beams from liquid metal ion sources*, Wiley, New York, 1991.
12. M. N. Huberman, *J. Appl. Physics*, 1970, **41**, 578-584.
13. B. P. Stimpson, D. S. Simons and C. A. Evans., *J. Phys. Chem.*, 1978, **82**, 660-670.
14. M. Cloupeau and B. Prunet-Foch, *J. Aerosol Sci.*, 1994, **25**, 1021-1036.
15. J. Fernández de la Mora, *J. Fluid Mech.*, 1992, **243**, 564-574.
16. J. Fernández de la Mora and I. G. Loscertales, *J. Fluid Mech.*, 1994, **260**, 155-184.
17. A. M. Gañan-Calvo, J. C. Lasheras, J. Davila and A. Barrero, *J. Aerosol Sci.*, 1994, **25**, 1121-1142.
18. J. Rosell-Llompart and J. Fernández de la Mora, *J. Aerosol Sci.*, 1994, **25**, 1093-1119.
19. A. Gañan-Calvo, *J. Fluid Mech.*, 1997, **335**, 165-188.
20. A. M. Gañan-Calvo, *J. Aerosol Sci.*, 1999, **30**, 863-872.

21. M. Gamero-Castaño, I. Aguirre-de-Carcer, L. de Juan and J. Fernández de la Mora, *J. Appl. Phys.*, 1998, **83**, 2428-2434.
22. M. Gamero-Castaño and J. Fernández de la Mora, *J. Chem. Phys.*, 2000, **113**, 815-832.
23. P. Lozano and M. Martinez-Sánchez, 38th AIAA/ASME/SAE/ASEE Joint Propulsion Conference & Exhibit, Indianapolis, IN, 2002.
24. M. Gamero-Castaño, *Phys. Rev. Lett*, 2002, **89**, 147602.
25. G. I. Taylor, *Proc. Royal Soc. A*, 1964, **280**, 383-397.
26. I. Romero-Sanz, R. Bocanegra, J. Fernandez de la Mora and M. Gamero-Castano, *J. Appl. Phys.*, 2003, **94**, 3599-3605.
27. M. Gamero-Castaño and V. Hruby, *J. Prop. Power*, 2001, **17**, 977-987.
28. Y. Chiu, B. L. Austin, R. A. Dressler, D. Levandier, P. T. Murray, P. Lozano and M. Martinez-Sanchez, *J. Prop. Power*, 2005, **21**, 416-423.
29. P. Lozano and M. Martinez-Sanchez, *J. Coll. and Interface Sci.*, 2005, **282**, 415-421.
30. P. Lozano, *J. Phys. D*, 2006, **39**, 126-134.
31. L. F. Velasquez-Garcia, M. Martinez-Sanchez and A. I. Akinwande, 40th AIAA/ASME/SAE/ASEE Joint Propulsion Conference and Exhibit, Fort Lauderdale, FL, 2004.
32. Y. Chiu and R. A. Dressler, in *Ionic Liquids: Not Just Solvents Anymore*, ed. R. Rogers, ACS Books, in press, Washington DC, Editon edn., 2006.
33. Y. Chiu, G. Gaeta, T. R. Heine and R. A. Dressler, 42nd AIAA/ASME/SAE/ASEE Joint Propulsion Conference & Exhibit, Sacramento, CA, 2006.
34. E. M. Knipping, M. J. Lakin, K. L. Foster, P. Jungwirth, D. J. Tobias, R. B. Gerber, D. Dabdub and B. J. Finlayson-Pitts, *Science*, 2000, **288**, 301-306.
35. B. C. Garrett, *Science*, 2004, **303**, 1146-1147.
36. P. B. Petersen and R. J. Saykally, *Annu. Rev. Phys. Chem.*, 2006, **57**, 12.11-12.31.
37. P. Jungwirth and D. J. Tobias, *J. Phys. Chem. B*, 2001, **105**, 10468-10472.
38. P. Jungwirth and D. J. Tobias, *J. Phys. B*, 2002, **106**, 6361-6373.
39. E. C. Brown, M. Mucha, P. Jungwirth and D. J. Tobias, *J. Phys. Chem. B*, 2005, **109**, 7934-7940.

40. M. Mucha, T. Frigato, L. M. Levering, H. C. Allen, D. J. Tobias, L. X. Dang and P. Jungwirth, *J. Phys. Chem. B*, 2005, **109**, 7617-7623.
41. L. X. Dang, *J. Phys. Chem. B*, 2002, **106**, 10388-10394.
42. L. X. Dang and T. M. Chang, *J. Phys. Chem. B*, 2002, **106**, 235-238.
43. S. Ghosal, J. C. Hemminger, H. Bluhm, B. S. Mun, E. L. D. Hebenstreit, G. Ketteler, D. F. Ogletree, F. G. Requejo and M. Salmeron, *Science*, 2005, **307**, 563-566.
44. E. A. Raymond and G. L. Richmond, *J. Phys. Chem. B*, 2004, **108**, 5051-5059.
45. D. F. Liu, G. Ma, L. M. Levering and H. C. Allen, *J. Phys. Chem. B*, 2004, **108**, 2252-2260.
46. P. B. Petersen, J. C. Johnson, K. P. Knutsen and R. J. Saykally, *Chem. Phys. Lett.*, 2004, **397**, 46-50.
47. P. B. Petersen and R. J. Saykally, *Chem. Phys. Lett.*, 2004, **397**, 51-55.
48. P. B. Petersen and R. J. Saykally, *J. Amer. Chem. Soc.*, 2005, **127**397, 15446-15452.
49. P. B. Petersen, R. J. Saykally, M. Mucha and P. Jungwirth, *J. Phys. Chem. B*, 2005, **109**, 10915-10921.
50. V. Znamenskiy, I. Marginean and A. Vertes, *J. Phys. Chem. A*, 2003, **107**, 7406-7412.
51. M. Moseler and U. Landman, *Science*, 2000, **289**, 1165-1169.
52. D. Duft, T. Achtzehn, R. Müller, B. A. Huber and T. Leisner, *Nature*, 2003, **421**, 128-128.
53. D. Duft, H. Lebius, B. A. Huber, C. Guet and T. Leisner, *Phys. Rev. Lett*, 2002, **89**, 084503.
54. R. L. Grimm and J. L. Beauchamp, *J. Phys. Chem. B*, 2005, **109**, 8244-8250.
55. R. L. Grimm and J. L. Beauchamp, *J. Phys. Chem. B*, 2003, **107**, 14161 -14163.
56. H. A. Stone, J. R. Lister and M. P. Brenner, *Proc. Royal Soc. London A*, 1999, **455**, 329-347.
57. L. F. Greengard, *The rapid evaluation of potential fields in particle systems*, The MIT Press, Cambridge, MA, 1988.
58. M. P. Allen and D. J. Tildesley, *Computer simulation of liquids*, Clarendon, Oxford, 1987.
59. M. Svanberg, *Mol. Phys.*, 1997, **92**, 1085-1088.

60. E. D. Stevens, *Acta Cryst.*, 1978, **B34**, 544-551.
61. W. D. Cornell, P. Cieplak, C. I. Bayly, I. R. Gould, J. K. M. Merz, D. M. Ferguson, D. C. Spellmeyer, T. Fox, J. W. Caldwell and P. A. Kollman, *J. Amer. Chem. Soc.*, 1995, **117**, 5179-5197.
62. E. Sigfridsson and U. Ryde, *J. Comput. Chem.*, 1998, **19**, 377-395.
63. L. Perera, U. Essmann and M. L. Berkowitz, *J. Chem. Phys.*, 1994, **102**, 450-456.
64. M. J. Frisch, G. W. Trucks, H. B. Schlegel, G. E. Scuseria, M. A. Robb, J. R. Cheeseman, J. Montgomery, J. A., T. Vreven, K. N. Kudin, J. C. Burant, J. M. Millam, S. S. Iyengar, J. Tomasi, V. Barone, B. Mennucci, M. Cossi, G. Scalmani, N. Rega, G. A. Petersson, H. Nakatsuji, M. Hada, M. Ehara, K. Toyota, R. Fukuda, J. Hasegawa, M. Ishida, T. Nakajima, Y. Honda, O. Kitao, H. Nakai, M. Klene, X. Li, J. E. Knox, H. P. Hratchian, J. B. Cross, V. Bakken, C. Adamo, J. Jaramillo, R. Gomperts, R. E. Stratmann, O. Yazyev, A. J. Austin, R. Cammi, C. Pomelli, J. W. Ochterski, P. Y. Ayala, K. Morokuma, G. A. Voth, P. Salvador, J. J. Dannenberg, V. G. Zakrzewski, S. Dapprich, A. D. Daniels, M. C. Strain, O. Farkas, D. K. Malick, A. D. Rabuck, K. Raghavachari, J. B. Foresman, J. V. Ortiz, Q. Cui, A. G. Baboul, S. Clifford, J. Cioslowski, B. B. Stefanov, G. Liu, A. Liashenko, P. Piskorz, I. Komaromi, R. L. Martin, D. J. K. Fox, T., M. A. Al-Laham, C. Y. Peng, A. Nanayakkara, M. Challacombe, P. M. W. Gill, B. Johnson, W. Chen, M. W. Wong, C. Gonzalez and J. A. Pople, *Gaussian 03, Revision C.02*, (2004) Gaussian, Inc., Wallingford, CT.
65. R. A. Kendall, T. H. Dunning, Jr. and R. J. Harrison, *J. Chem. Phys.*, 1992, **96**, 6796-6806.
66. P. C. Hariharan and J. A. Pople, *Theoret. Chim. Acta*, 1973, **28**, 213-222.
67. M. N. Glukhovtsev, A. Pross and L. and Radom, *J. Am. Chem. Soc.*, 1995, **117**, 2024-2032.
68. A. D. Becke, *J. Chem. Phys.*, 1993, **98**, 5648-5652.
69. R. H. Hertwig and K. Wolfram, *Chem. Phys. Lett.*, 1997, **268**, 345-351.
70. P. J. Stephens, F. J. Devlin, C. F. Chabalowski and M. J. Frisch, *J. Phys. Chem.*, 1994, **98**, 11623-11627.
71. M. Head-Gordon and J. A. Pople, *Chem. Phys. Lett.*, 1990, **166**, 275-280.

72. J. A. Pople, J. S. Binkley and R. Jeeger, *Int. J. Quant. Chem. Symp.*, 1976, **10**, 1-19.
73. C. M. Aikens, S. P. Webb, R. L. Bell, G. D. Fletcher, M. W. Schmidt and M. S. Gordon, *Theor. Chem. Acc.*, 2003, **110**, 233-253.
74. R. Krishnan, J. S. Binkley, R. Seeger and J. A. Pople, *J. Chem. Phys.*, 1980, **72**, 650-654.
75. M. N. Glukhovtsev, A. Pross, M. P. McGrath and L. and Radom, *J. Chem. Phys.*, 1995, **103**, 1878-1885.
76. M. S. Gordon and M. W. Schmidt, in *Theory and Applications of Computational Chemistry*, eds. C. E. Dykstra, G. Frenking, K. S. Kim and G. E. Scuseria, Elsevier, Amsterdam, Editon edn., 2005.
77. M. W. Schmidt, K. K. Baldridge, J. A. Boatz, S. T. Elbert, M. S. Gordon, J. J. H., K. S., N. Matsunaga, K. A. Nguyen, S. Su, T. L. Windus, M. Dupuis and J. A. Montgomery, Jr., *J. Comput. Chem.*, 1993, **14**, 1347-1363.
78. L. Zhu, W. Chen, W. L. Hase and E. W. Kaiser, *J. Phys. Chem.*, 1993, **97**, 311-322.
79. M. T. Rodgers, K. M. Ervin and P. B. Armentrout, *J. Chem. Phys.*, 1997, **106**, 4499-4508.
80. T. S. Beyer and D. F. Swinehart, *Comm. Assoc. Comput. Machines*, 1973, **16**, 379.
81. W. D. Luedtke and U. Landman, to be published.
82. D. Li and A. W. Neumann, *J. Coll. and Interface Sci.*, 1992, **148**, 190-200.
83. L. Perera and M. L. Berkowitz, *J. Chem. Phys.*, 1991, **95**, 1954-1963.
84. P. Ayotte, S. B. Nielsen, G. H. Weddle, M. A. Johnson and S. S. Xantheas, *J. Phys. Chem. A*, 1999, **103**, 10665-10669.
85. D. S. Simons, B. N. Colby and J. C. A. Evans, *Int. j. Mass Spect. Ion Phys.*, 1974, **15**, 291-302.

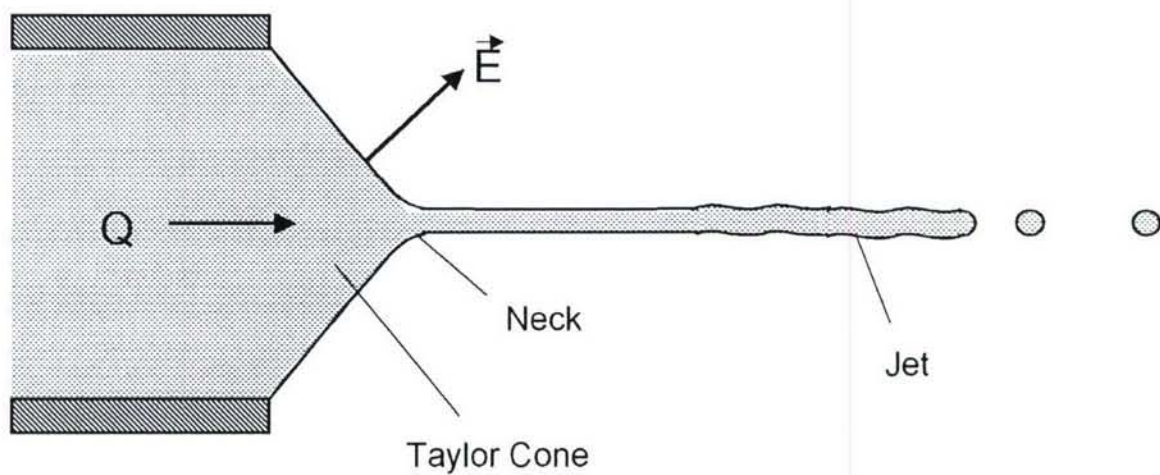


fig1.

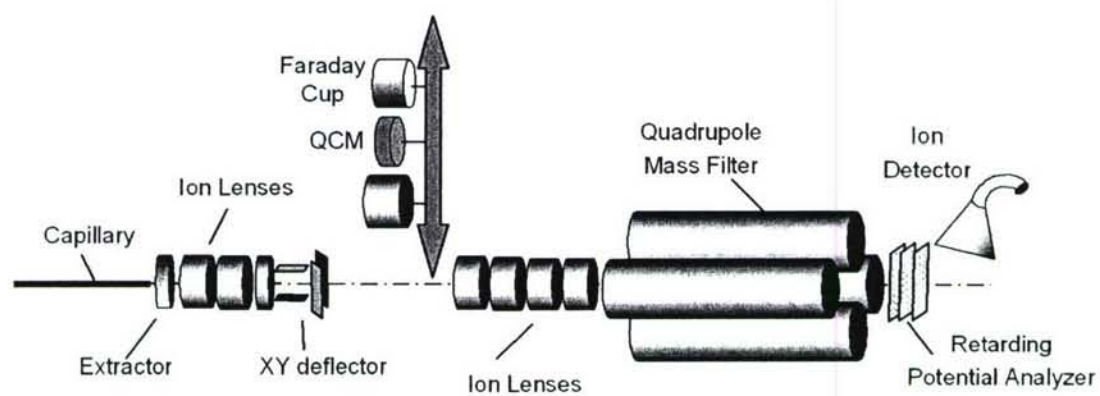


Fig 2.

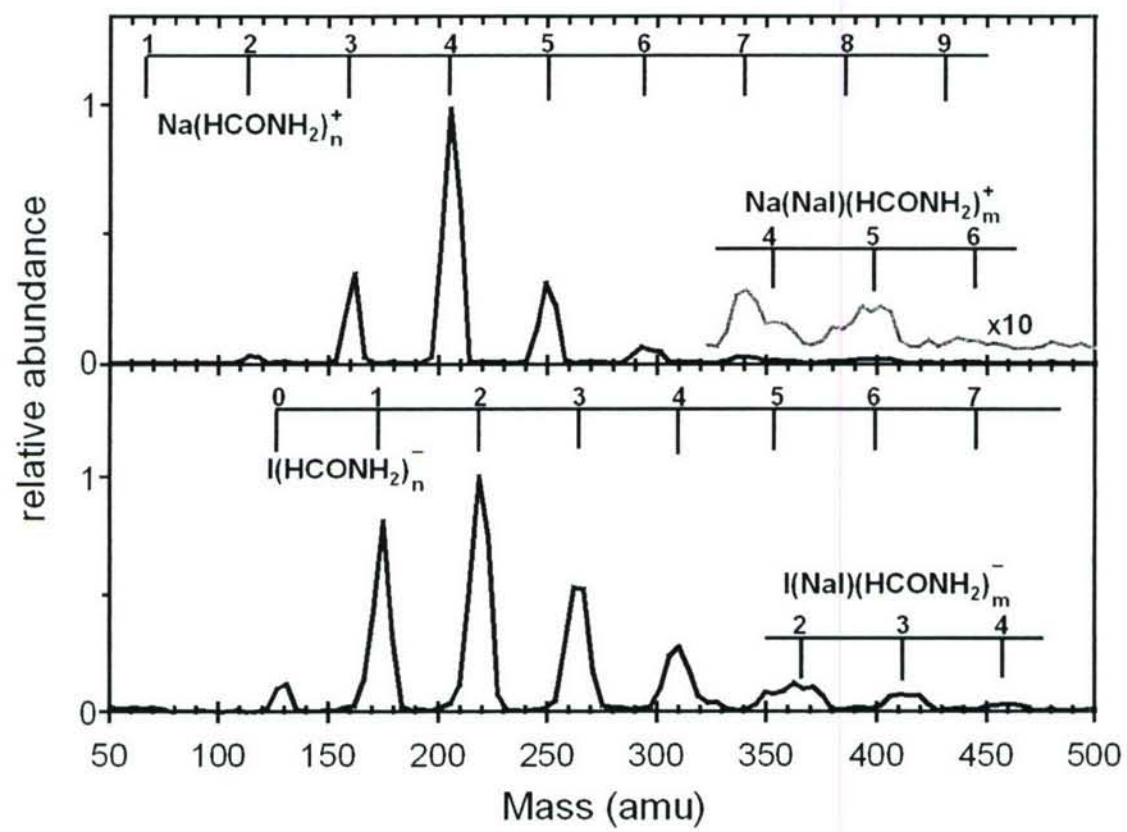


Fig 3.

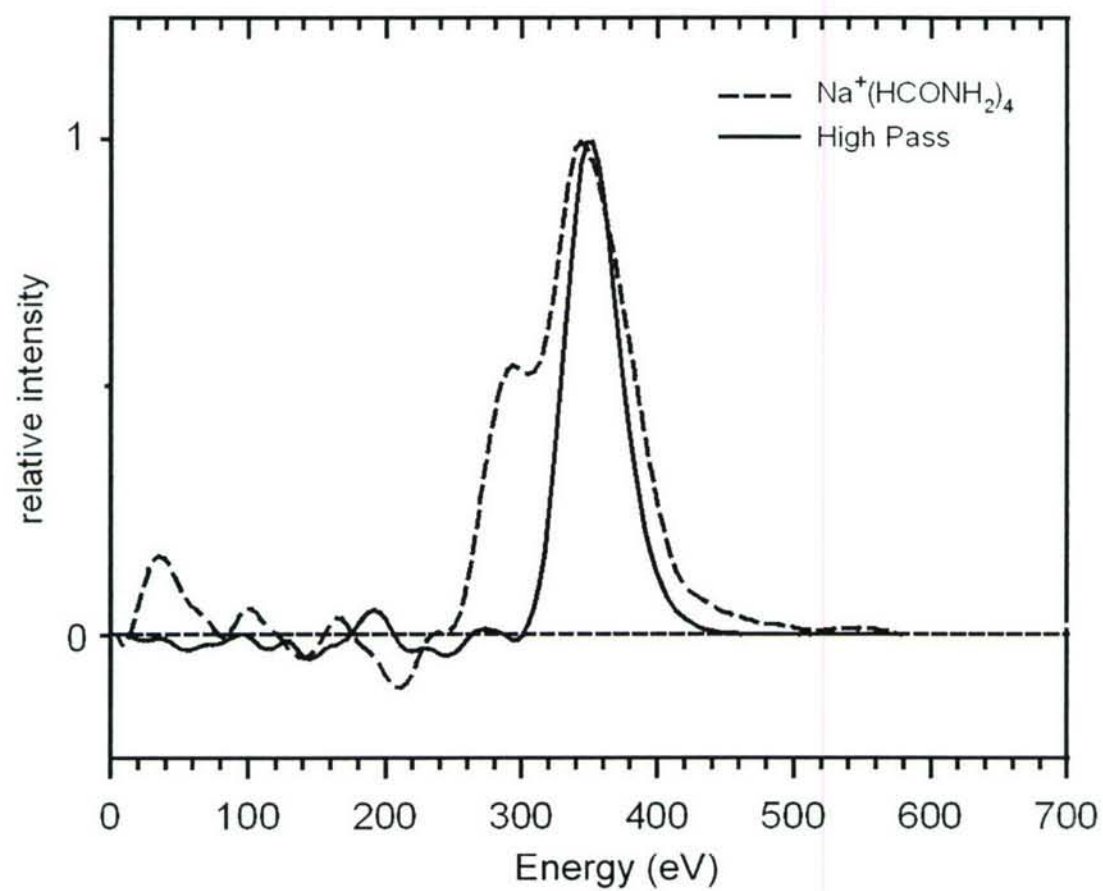


Fig 4.

field induced elongation of formamide droplet

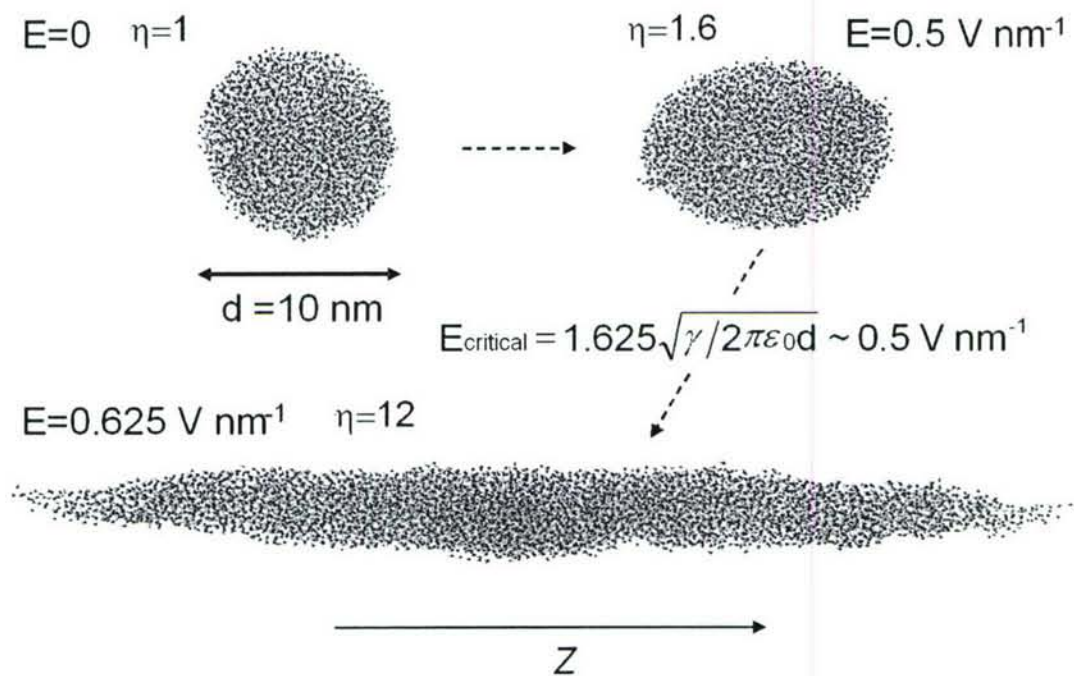


Fig 5.

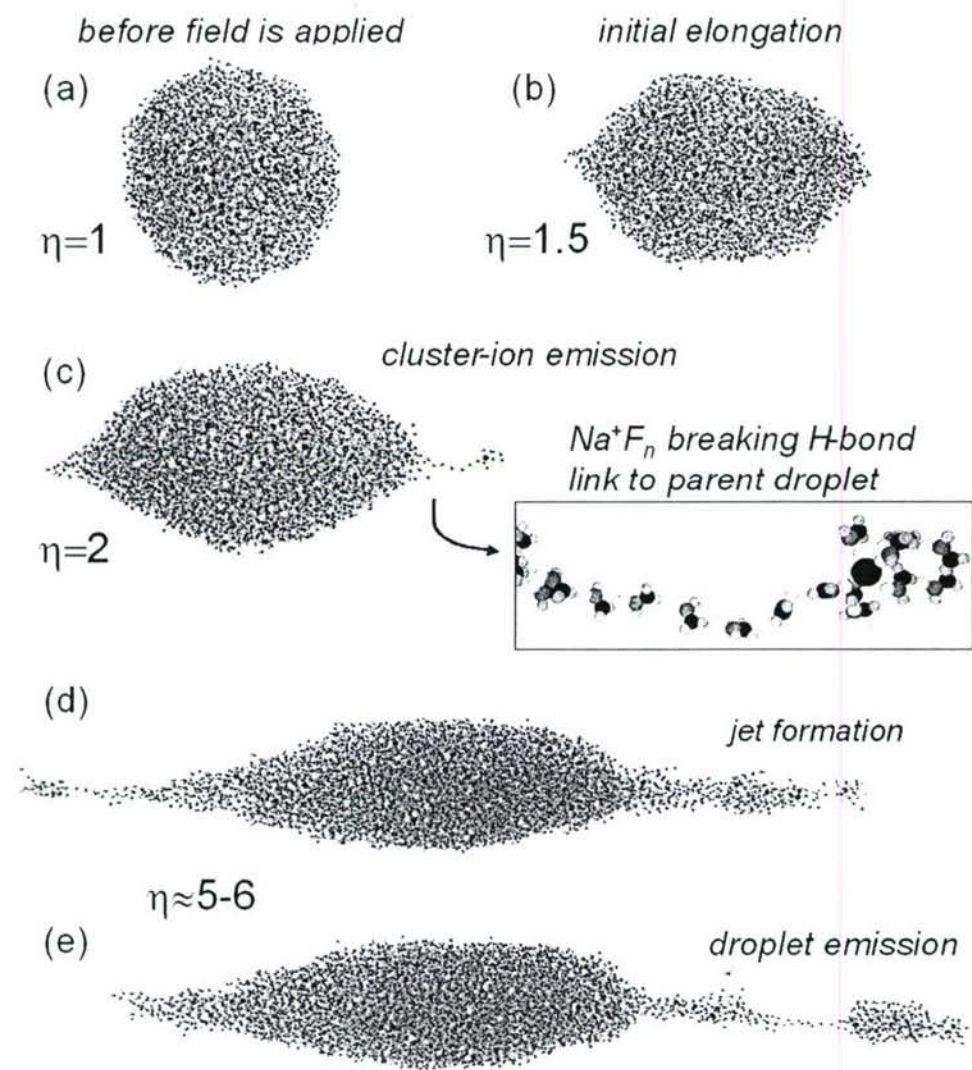


Fig 6.

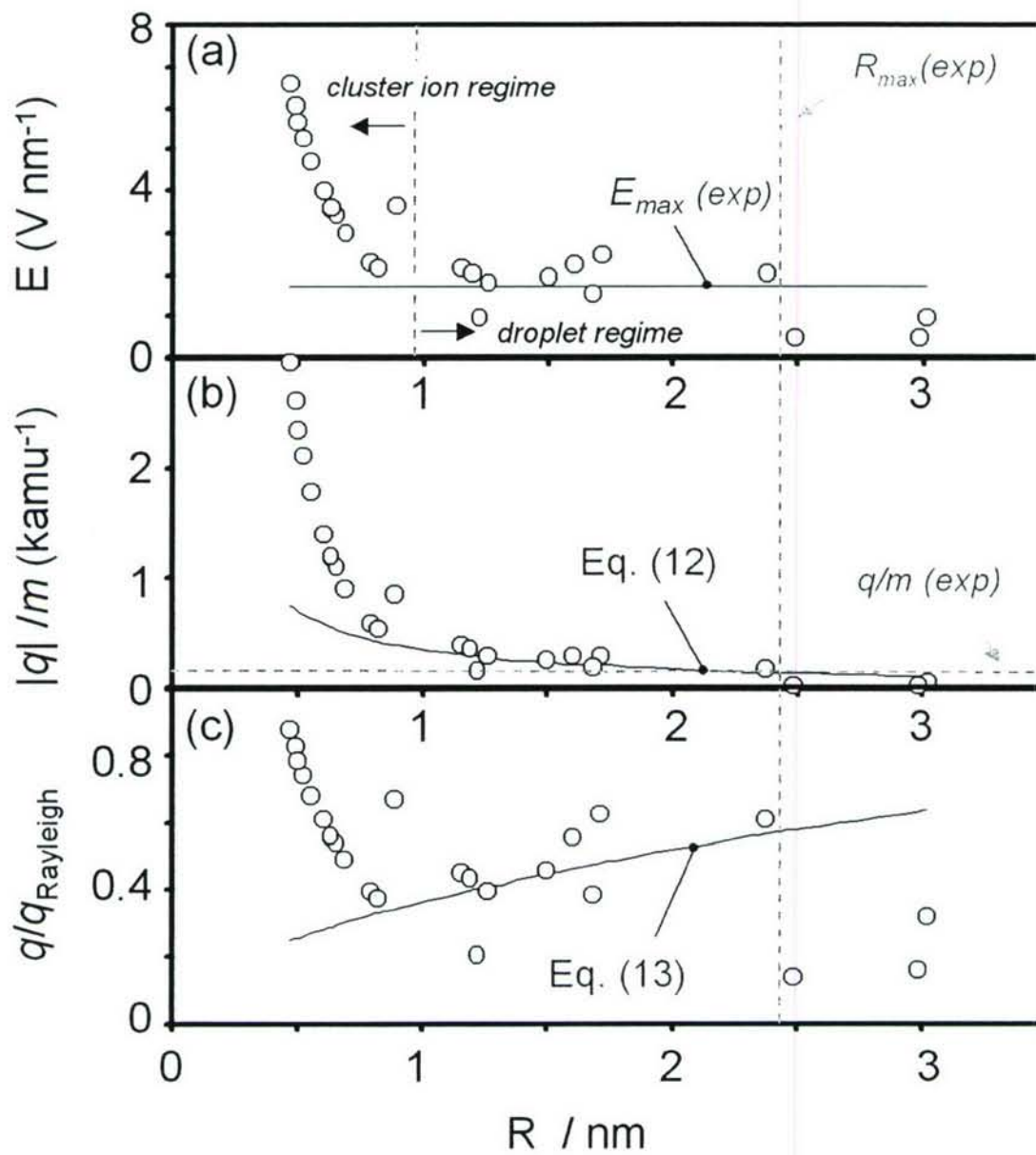


Fig 7.

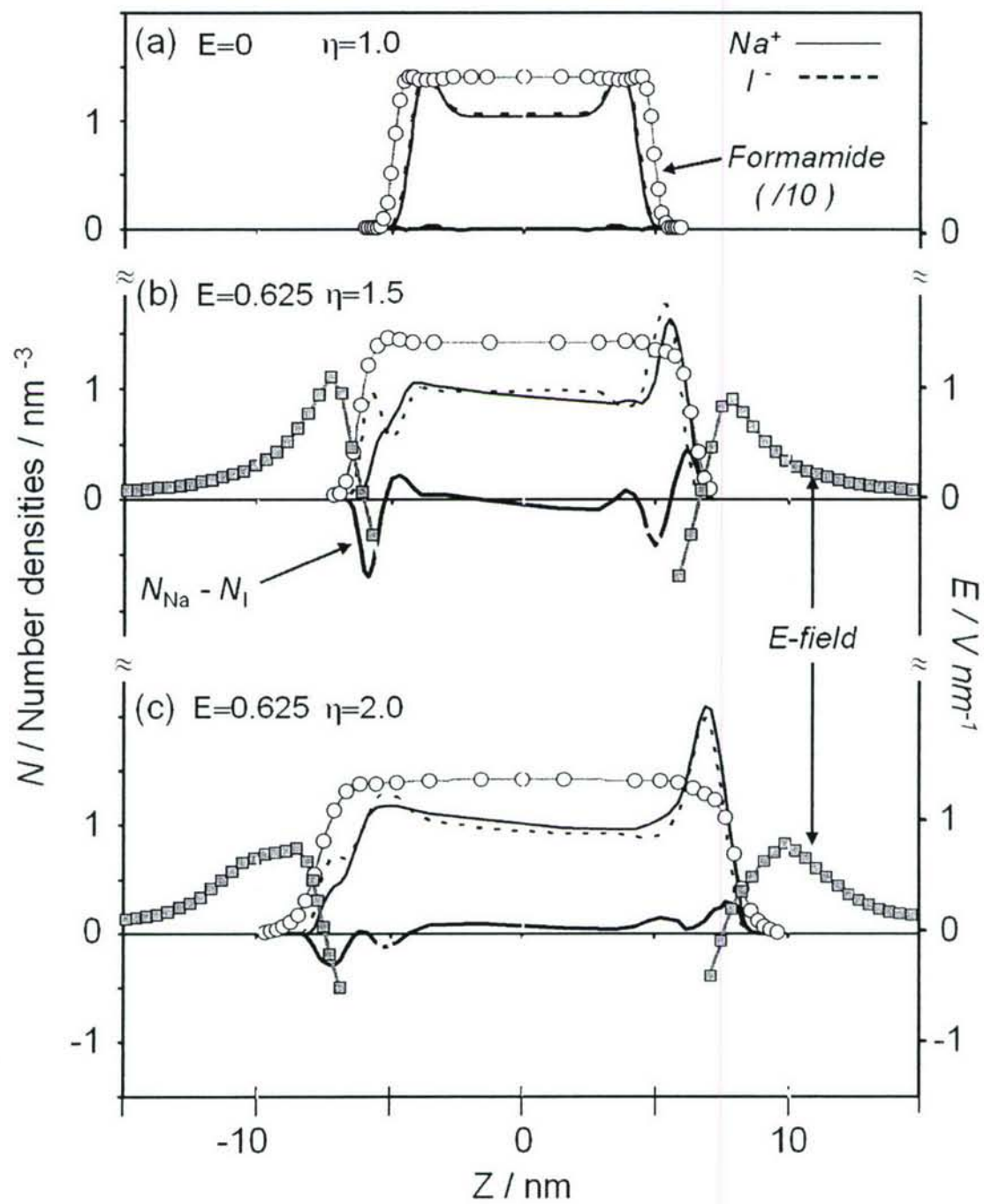


Fig 8.

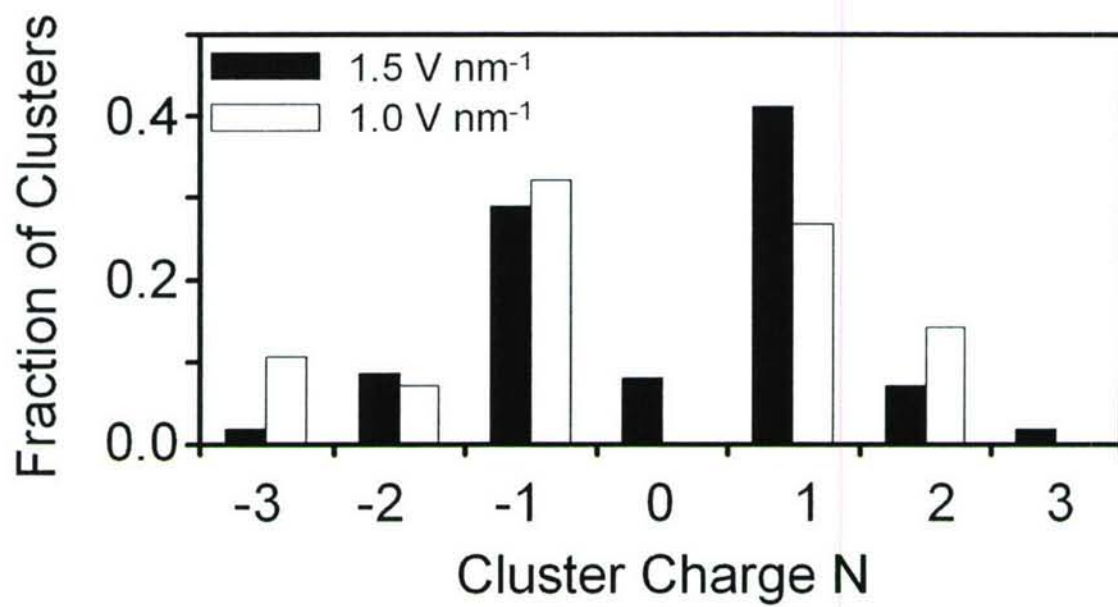


Fig 9.

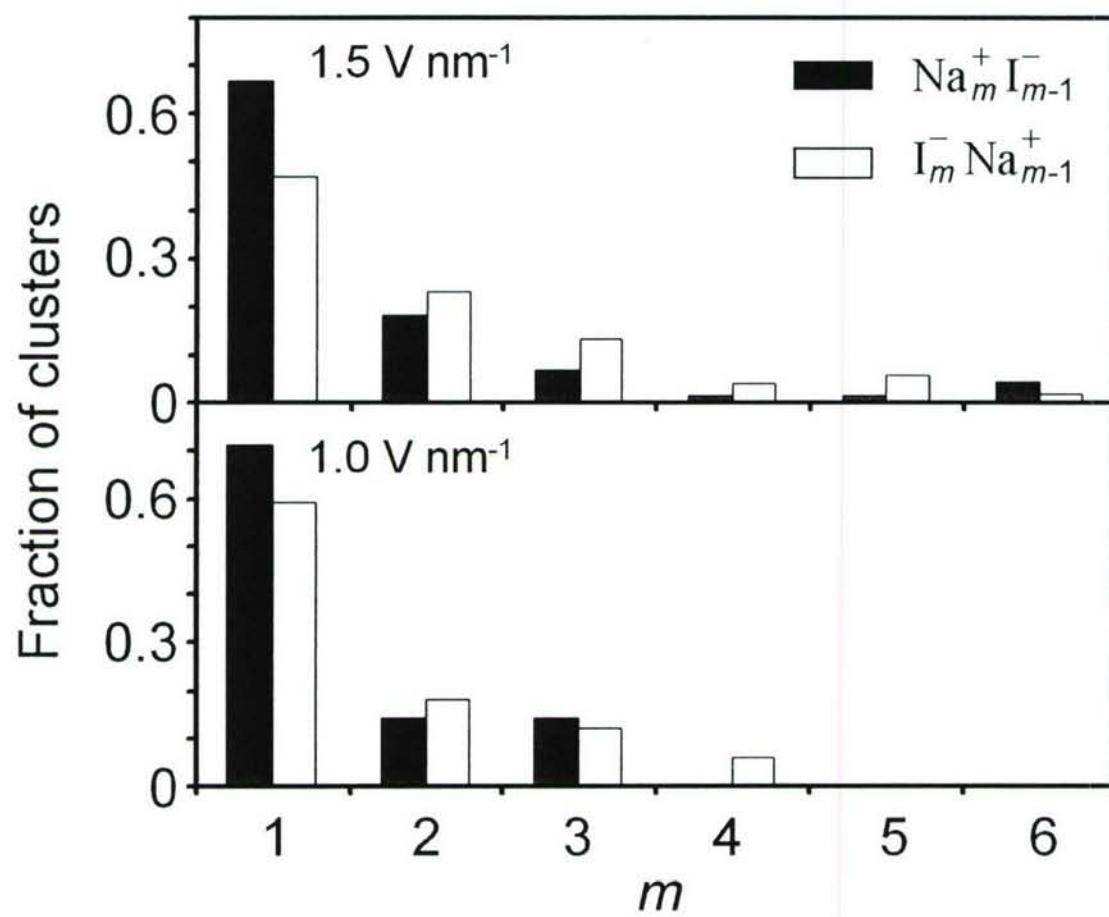


Fig 10.

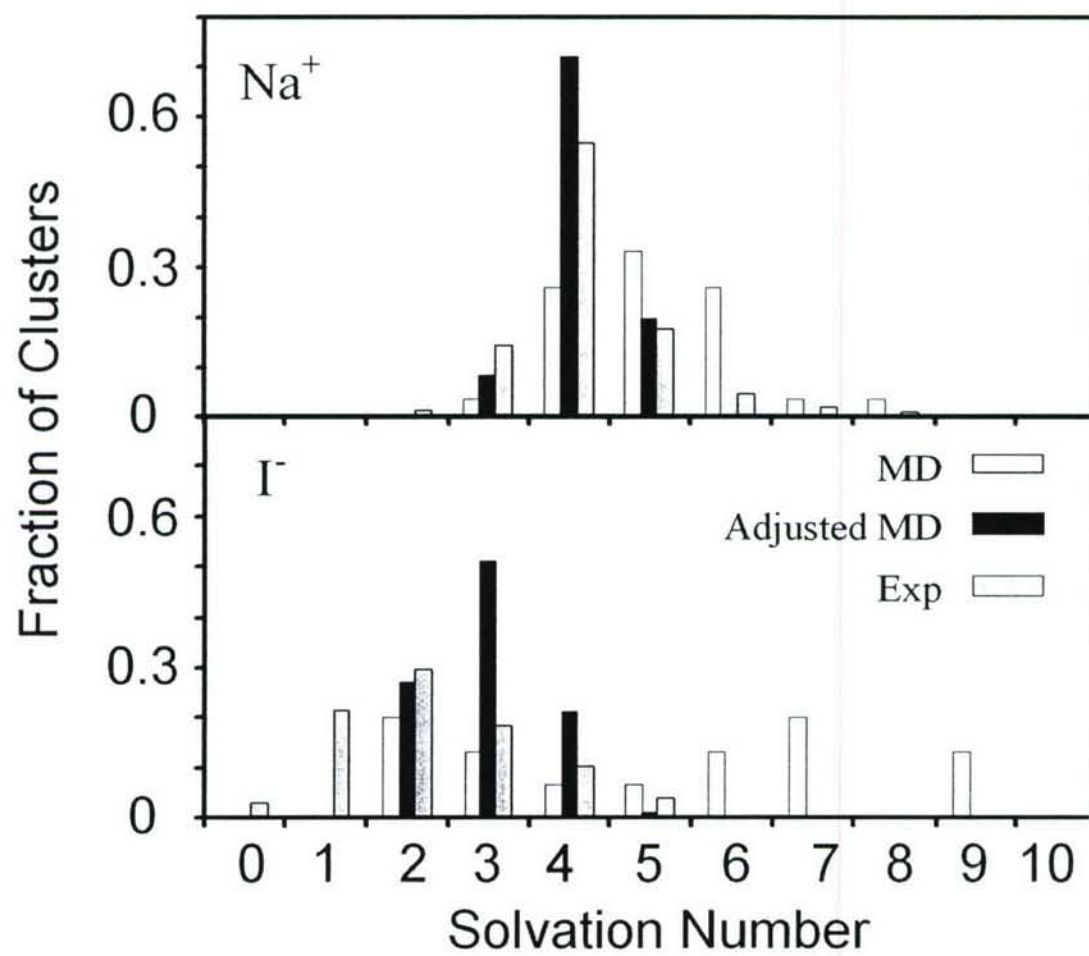


Fig 11